工學博士學位論文

Fabrication of electrospun polyacrylonitrile nanofibers based transducer for chemical/biosensors application

전기방사 폴리아크릴로니트릴 나노섬유 기반 트랜스듀서 제조 및 화학/바이오센서로의 응용

2020年 2月

서울大學校 大學院

化學生物工學部

金 佑 永

Fabrication of electrospun polyacrylonitrile nanofibers based transducer for chemical/biosensor application

전기방사 폴리아크릴로니트릴 나노섬유 기반 트랜스듀서 제조 및 화학/바이오센서로의 응용

指導敎授 張 正 植

이 論文을 工學博士 學位論文으로 提出함

2019 年 11 月

서울大學校 大學院

化學生物工學部

金 佑 永

金佑永의 工學博士 學位論文을 認准함

2019 年 11 月

委 員 長 _____ (印)

副委員長 _____ (印)

委 員 _____ (印)

委 員 _____ (印)

委 員 _____ (印)

Fabrication of electrospun PAN nanofibers based transducer for chemical/biosensor application

by

Wooyoung Kim

Submitted to the Graduate School of Seoul National University in Partial Fulfillment of the Requirements for the Degree of Doctor of Philosophy

October, 2019

Thesis Adviser: Jyongsik Jang

Abstract

In recent decades, there has been tremendous researches for developing one-dimensional (1D) nanomaterials used for sensor transducer, owing to their structural properties such as high aspect ratio and high specific surface area. Among diverse method to fabricate 1D nanomaterials, electrospinning has been widely utilized because of their simple usage and low operating temperature. Additionally, because the manufactured fibers come in a mat form, various applications are possible in itself. Although, multifarious synthesis methods have been studied to prepare 1D nanomaterials *via* electrospinning, Research into the decoration of metals or metal oxides on the surface of nanofibers and method of carbonize nanofibers to produce flexible and free-standing mats are still lacking.

This dissertation proposes the method to prepare diverse electrospun polyacrylonitrile nanofibers (PAN NFs) based composite materials for sensor application by decoration of metal or metal oxide and additional carbon. Firstly, shape controlled palladium nanoflower decorated polypyrrole/PAN NFs (Pd_PPy/PAN NFs) were prepared using electrospinning of PAN solution followed by polypyrrole vapor

deposition polymerization (VDP) and electrodeposition of palladium nanoflowers. The shape of palladium was determined by controlling the sulfuric acid concentration in electrolyte during electrodeposition, and applied as a hydrogen peroxide sensor electrode material.

Secondly, chemical vapor deposition (CVD) and metal etching were adopted to decorate copper (Cu) derived carbon on carbon nanofiber (CNF). The structure of Cu derived carbon was determined by the type of Cu used, and protrusion shape was produced on CNFs when sphere type Cu was used. Then, platelet derived growth factor (PDGF)-B binding aptamer was immobilized on as prepared materials and applied as PDGF biosensor with high sensitivity and selectivity.

Finally, to fabricate manganese dioxide decorated carbon nanofiber (Mn@CNF), potassium permanganate was used as a precursor and chemically reduced by stirring and heat treatment. Using Mn@CNF as a transducer for sensor, the nerve gas agent simulant (DMMP) was detected with ultrasensitive.

In addition, the fact that the material produced in this dissertation exhibits electrical resistance and target analyte sensing performance that does not diminish despite of bending, offers the potential for flexible and free-standing substrate for sensor application.

Keywords: polyacrylonitrile; electrospinning; one-dimensional nanomaterials; carbon nanofiber; polypyrrole; flexible substrate; sensor

Student Number: 2015-21014

List of Abbreviations

%: percent

1D: one-dimensional

A: ampere

Ag/AgCl: silver/silver chloride

APS: ammonium persulfate

ATP: adenosine triphosphate

Au: gold

BSA: bovine serum albumin

℃: celsius degree

ca. circa

Cal.: calmodulin

CH_4: methane

CP: conducting polymer

Cu: copper

CuC/CNF: copper derived carbon/CNF

CVD: chemical vapor deposition

DMF: N,N-dimethyl formamide

DMMP: dimethyl methylphosphonate

DMT-MM: 4-(4,6-Dimethoxy-1,3,5-triazin-2-yl)-4-methyl morpholinium chloride

EDX: energy-dispersive X-ray spectroscopy

eV: electronvolt

f: femto

FE-SEM: Field-emission scanning electron microscope

Fe: iron

$FeCl_3$: iron (III) chloride

FET: field-effect-transistor

FlakeC/CNF: flake type copper derived carbon/CNF

H_2: hydrogen gas

H_2O_2: hydrogen peroxide

H_2S: hydrogen sulfide

H_2SO_4: sulfuric acid

HR-TEM: high-resolution

i.e.: Id Est

I: current

I_0: initial resistance

$KMnO_4$: potassium permanganate

$KMnO_4$: potassium permanganate

L: liter

LED: light-emitting diode

m: meter

M: molar concentration

min: minute

Mn@CNF: manganese dioxide decorated carbon nanofibers

M_w: molecular weight

n: nano

NADPH: nicotinamide adenine dinucleotide phosphate

NH_3: ammonia

NO_2: nitrogen dioxide

OER: oxygen evolution reaction

ORR: oxygen reduction reaction

p-type: positive type

p: pico

PAN NFs: polyacrylonitrile nanofibers

PAN: poly (acrylonitrile)

PANI: polyaniline

PBS: phosphate buffer saline

Pd: palladium

Pd_PPy/PAN NFs: palladium decorated polypyrrole/polyacrylonitrile nanofibers

$PdCl_2$: palladium (II) chloride

PDGF: Platelet-derived growth factor

PDMS: Polydimethylsiloxane

PEDOT: poly(3,4-ethylenedioxythiophene)

PET: polyethylene terephthalate

PI: polyimides

PPy: polypyrrole

Pt: platinum

PVA: poly (vinyl alcohol)

PVP: poly (vinyl pyrrolidine)

ROS: reactive oxygen species

S/N: signal to noise

s: second

S: sensitivity

sccm: standard cubic centimeters per minute

SO_4^{2-}: sulfate ion

SP10C/CNF: sphere type copper derived carbon/CNF

TEM: transmission electron microscopy

V: voltage

VDP: vapor phase deposition

w/: with

w/o: without

XPS: X-ray photoemission spectroscopy

XRD: X-ray diffraction

μ: micro

List of Figures

Figure 51. Resistance change of Mn@CNF with repetitive bending.

List of Tables

Table of Contents

1. Introduction

1.1 Background

1.1.1. Conducting polymer

Conduction polymers (CPs) have attracted a great attention in past few decades. Since the discovery of polyacetylene in the 1970s [1], many researches have been conducted on various CPs polymers such as polypyrrole (PPy), polyaniline (PANI), and poly(3,4-ethylenedioxythiophene) (PEDOT) (**Figure 1**) [2-3]. The backbone of the CPs has a structure in which single (σ bond) and double (π bond) bonds repeated. This pi-pi conjugated system allows the pi electrons to move freely, giving the polymer excellent electrical and optical properties. Due to their distinctive properties, CPs have been applied to various applications such as light emitting diode (LED), solar cell, energy storage device, fuel cell, transistor and especially used as transducer for diverse kinds of sensor [4]. Furthermore, CPs can also be applied to polymer field-effect-transistor (FET) using semiconductor feature. On this occasion, most CPs operate p-channel FETs because holes move faster than electrons.

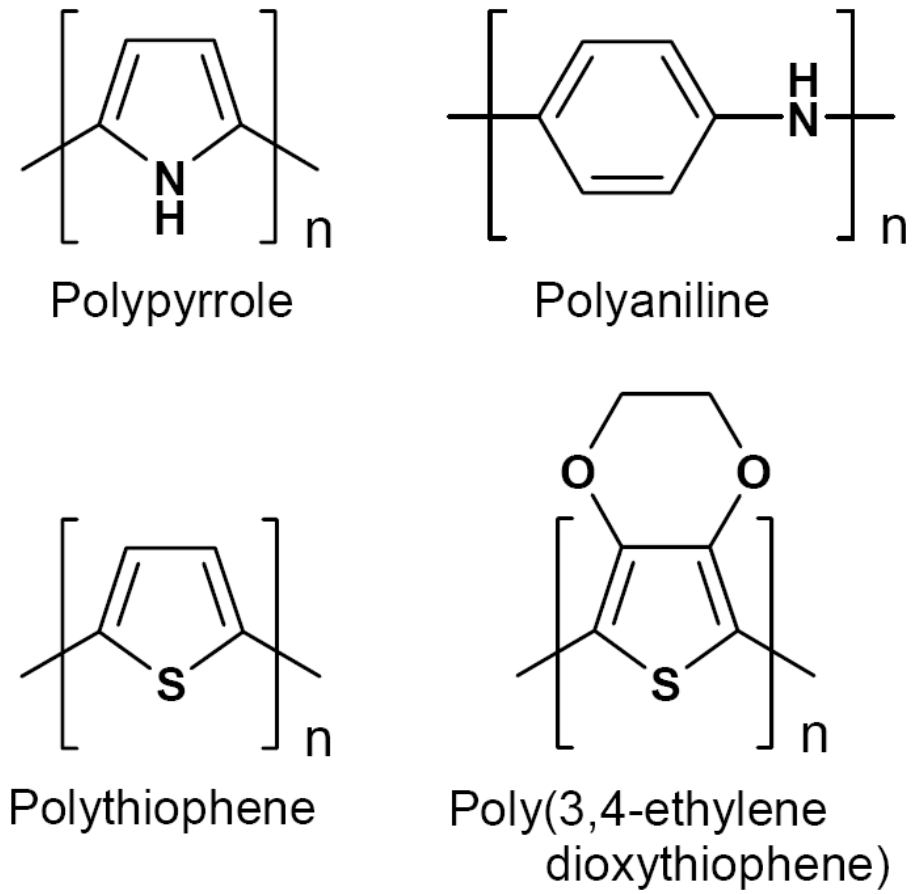

Figure 1. Typical structure of conducting polymers [5].

1.1.1.1. Polypyrrole

Among CPs, PPy is one of the best known conducting polymers composed of five membered heterocyclic ring [6]. Due to its high electrical conductivity, redox property, and environmental stability, it is widely used as a transducer for sensors. PPy can be easily prepared by several methods such as electrochemical polymerization and chemical approaches in both aqueous and non-aqueous solutions [7-10]. In the case of the electrochemical polymerization method, PPy is grown on a conductive substrate, whereas in the chemical method, the polymerization proceeds in such a way that Py monomer in the gas phase or liquid phase reacts with oxidant to generate powder.

The repeating unit of produced PPy chains is predominantly α-α coupling and thus the PPy chains structure is intrinsically linear and planar. However, conformational and structural defects are also generated during PPy polymerization. The conformational defects are caused by irregular rotation of α-α bonds and the structural defects are caused by α-β bonds, hydroxyl groups, and carbonyl groups. The α-β bonds are formed by crosslinking or bracing of polymer chains, and hydroxyl and carbonyl groups are produced by overoxidation (**Figure 2**).

These defects shorten the conjugation length of the polymer chain and cause aggregation of the nanomaterials [11].

PPy has four different electronic band structures at the doping level of the polymer chain. In neutral state, PPy behaves like an insulator with a large band gap energy of 3.16 eV. However, in the polymerization process, PPy chains have electroneutrality because they are doped with counter ions. (mostly anions). When a negative charge is extracted from the component of PPy chain by the doping process, benzenoid to quinoid structural changes in local deformation result in a polaron state. [12]

The formation of polarons creates two localized electronic levels (bonding and antibonding) between the band gaps while the unpaired occupied the bonding state. (S = 1/2) Further negative charge extraction leads to the formation of a double charged bipolaron. As oxidative doping proceeds more and more (a doping level of *ca*. 33 %), two narrow bipolaronic bonds are formed (**Figure 3** and **4**).

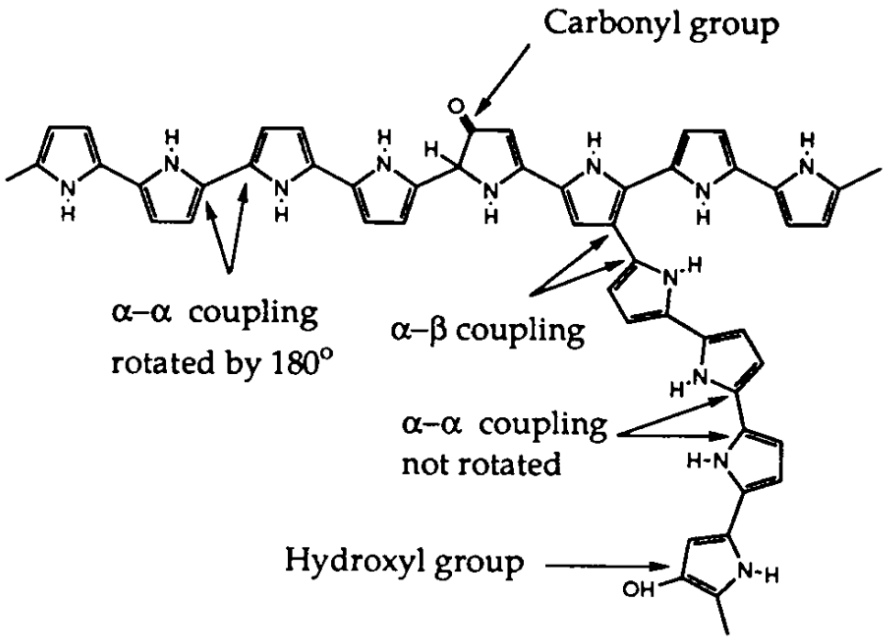

Figure 2. Feasible polymer structures in polypyrrole chains [11].

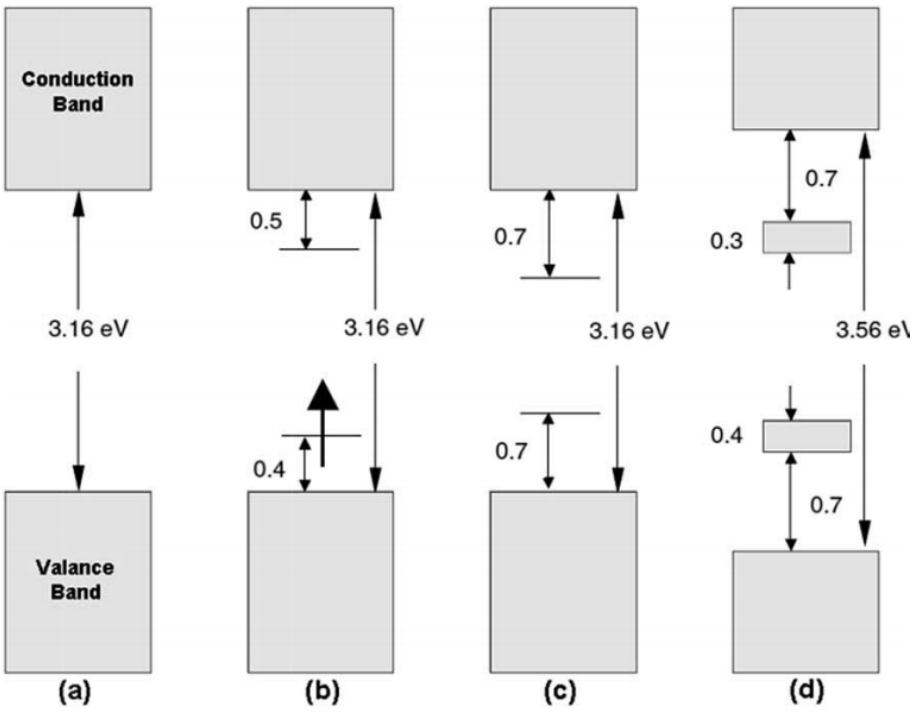

Figure 3. Electric energy diagrams for (a) neutral, (b) polaron, (c) bipolaron, and (d) fully doped polypyrrole [12].

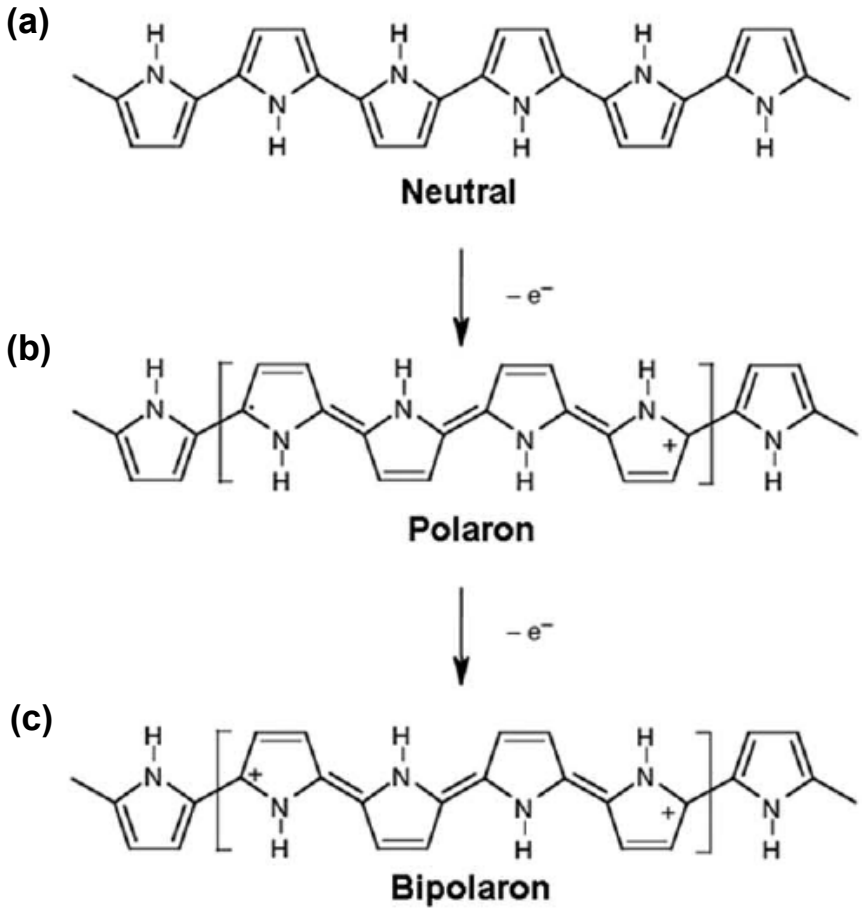

Figure 4. Electronic structures of (a) neutral, (b) polaron in partially doped, and (c) bipolaron in fully doped polypyrrole [12].

1.1.1.2. Vapor deposition polymerization (VDP)

Vapor deposition process has been used mainly in the coating industry. Various methods have been developed to enable high quality coatings. In addition, it has been widely studied because it has the advantage of coating to a desired substrate. The vapor deposition polymerization (VDP) is a type of vapor deposition that polymerizes gas monomers in a coating form. VDP is not only able to coat polymers uniformly, but also can be applied to various types of coatings by changing polymerization conditions such as pressure and temperature, which is widely used in nanomaterials manufacturing. Typically, the organic-organic or inorganic-organic core-shell nanomaterials could be readily prepared by VDP method. Various kinds of initiators are used for the polymerization, such as iron (III) chloride ($FeCl_3$) or ammonium persulfate (APS) (**Figure 5**) [13-19].

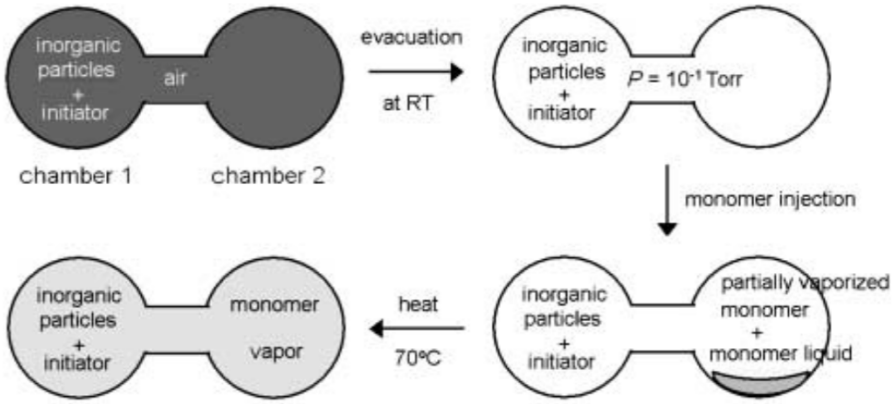

Figure 5. Schematic diagram of vapor deposition polymerization process [20].

1.1.2. One-dimensional nanomaterials

Advances in science and technology have enabled the development of smaller, lower-level materials. In this context, research into developing nanomaterials has continued to improve performance and apply them to appropriate applications. In general, dimensions of nanomaterials can be classified as zero, one, two, and three (**Figure 6**). Among those materials, one-dimensional (1D) nanomaterials have received much attention due to their intrinsic characteristic and potential in various applications such as energy conversion/storage device, catalyst, and sensors [21-24]. The morphological features of the 1D material not only enable more efficient charge-carrier movement in the long axis direction, but also have a high surface area due to the high aspect ratio. As an element building block of such nanostructures, 1D nanomaterials such as nanofibers, nanotubes, nanoneedles, nanowires, and nanoribbons played critical role to construct advanced nanostructures (**Figure 7**) [25-26].

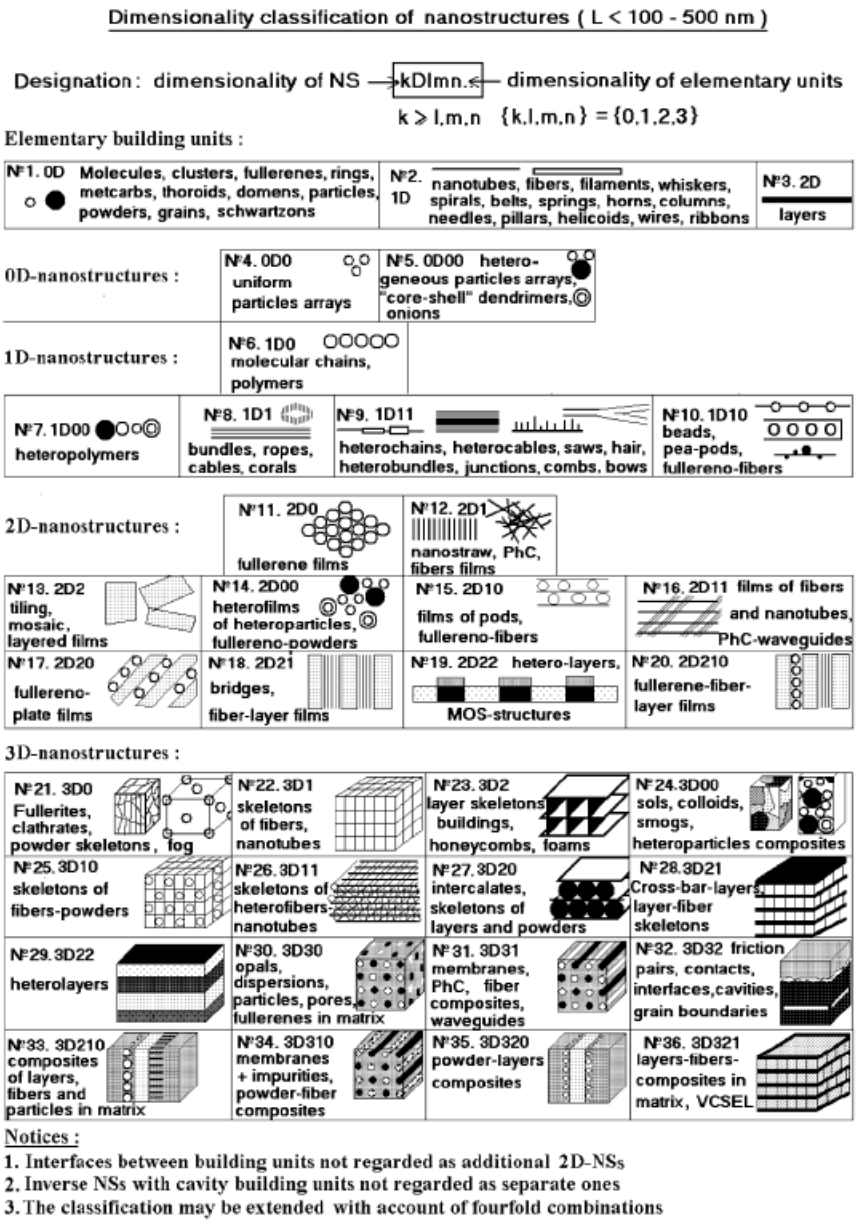

Figure 6. Example of nanostructure depend on dimension [27].

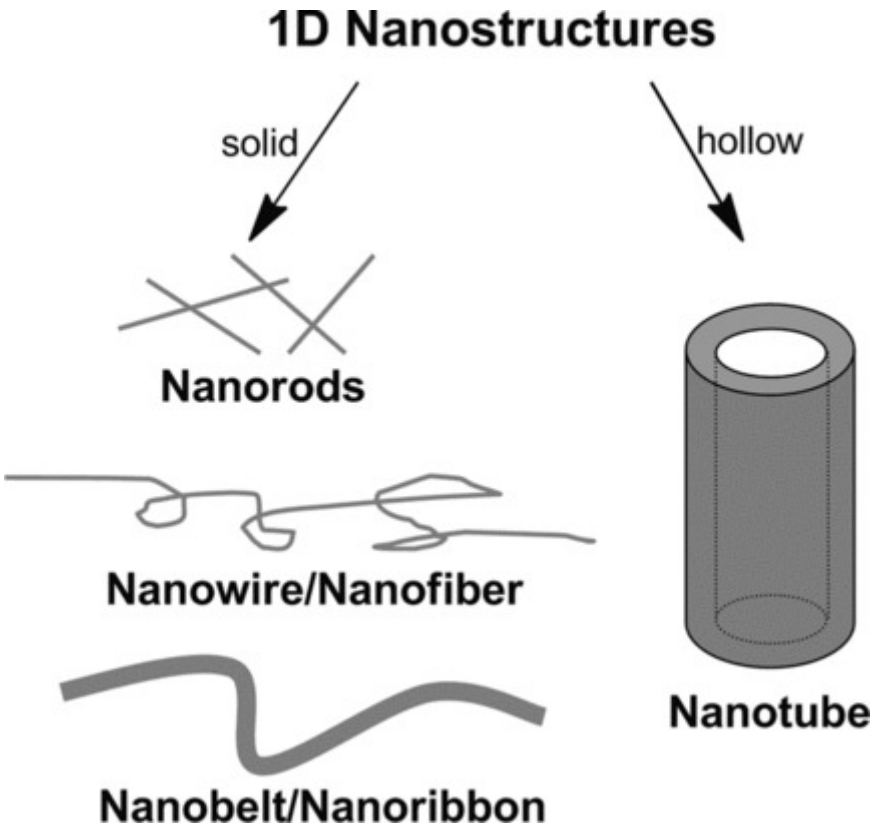

Figure 7. Classification of 1D nanostructures [28].

1.1.2.1. Electrospinning

Electrospinning is a facile and simple way to fabricate 1D materials of various sizes. It shares the features of electrospray and conventional solution dry spinning but does not require high temperature. Instead, apply high electric force to the polymer droplet to extract the nanofibers. Applying a sufficient voltage to the metal needle creates a charge inside the polymer droplet. The droplet stretched when the applied charge exceeds the surface tension of the polymer solution. When beyond the critical point, the stream of liquid erupts at the surface. If the molecular cohesion of the liquid is high enough, no liquid stream breakage occurs and the charged polymer liquid jet is forms. The generated liquid jet is received by the collector in the form of fiber through elongation and thinning (**Figure 8**) [29-30].

The nanofiber produced by electrospinning can be tuned by adjusting various parameters such as polymer solution concentration, applied voltage, atmosphere condition and needle type. In addition, various kinds of nanofibers could be prepared by using mixed polymer solution or metal oxide precursor/polymer solution. Lately, method of preparing carbon or metal oxide/carbon nanofibers based on heat treatment of electrospun nanofiber is widely studied (**Figure 9**) [31-32].

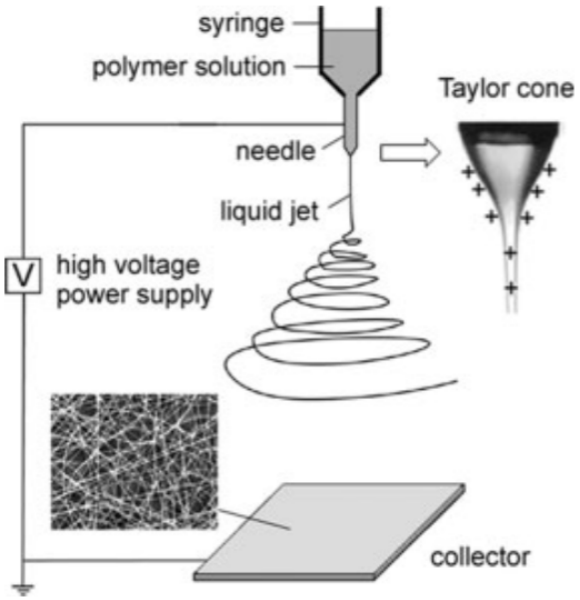

Figure 8. schematic diagram for preparing electrospun nanofibers *via* electrospinning [33].

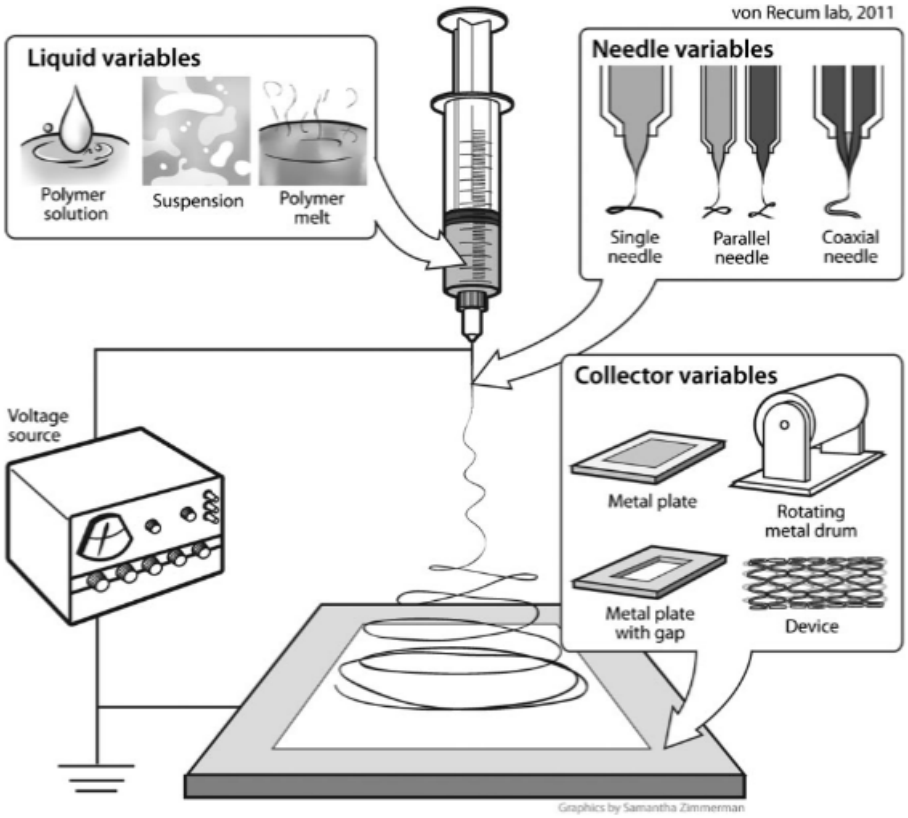

Figure 9. Schematic diagram of diverse variables affecting electrospinning [34].

1.1.2.2. Electrospun polymer derived carbon nanomaterials

Research using various kinds of electrospun nanofibers as a carbon source has been widely conducted. Various polymers are used as carbon sources such as poly (vinyl alcohol) (PVA), polyimides (PI), poly (vinyl pyrrolidone) (PVP), and poly (acrylonitrile) (PAN) [35-39]. Electrospun nanofibers become carbon nanofibers through a stabilization process that transforms the aliphatic chain structure into a ring form and carbonization at about 1000 ℃. Without thermal stabilization, the cross linking process will not proceed and the constitution of the carbon nanofibers may collapse. The collapse of the nano-scale structure can lead to mechanical property degradation at the micro-scale, which obstructs the use of electrospun nanofibers in the form of mats. Among various polymers, PAN received great interest as carbon source owing to their high degradation temperature in air condition. This allows stabilization at higher temperatures and easier chemical treatment compared to polymers such as PVP and PVA [40-41]. In addition, the nitrogen in the molecular structure remains after carbonization, making n doping carbon nanofibers. In recent years, research has been carried out to change the structure and porosity using various methods such as polymer solution mixing and chemical vapor deposition (CVD).

1.1.3. Composite materials

In the last few years, interest in organic-inorganic composite materials in research and industrial fields has increased. This method leads to improvement of chemical and mechanical properties of materials [42-43]. Additionally, mutual complementary interaction could offset each drawback. For this reason, research has been conducted on the manufacture of composite materials of various combinations and types such as metal/polymer, metal/polymer, metal oxide/carbon. In the case of energy storage devices, inorganic materials have a large theoretical capacity but poor durability. Meanwhile, organic materials are stable but have a smaller capacity than inorganic materials. However, in case of composite materials are used, high capacity and stability can be achieved at the same time. In the case of chemiresistive sensors, inorganic materials have a high operating temperature, and organic materials have por stability. Inorganic materials have high sensitivity but have the disadvantage of requiring high temperature to operating properly. Meanwhile, organic based sensors have fast response/recovery behavior with disadvantage of poor stability which hinder the using as sensors. Therefore, using composite materials as transducers of sensors can enable more efficient operation at room temperature [44-48].

1.1.3.1. Noble metal/conducting polymer composite materials

Noble metal such as gold (Au), platinum (Pt), palladium (Pd) have been received much attention because of their intrinsic properties that turned up at nano-scale. Among them, catalytic characteristics are applied to various fields such as non-enzyme sensors, automobile exhaust catalysts, oxygen evolution reaction (OER), and oxygen reduction reaction (ORR). In particular, Pd plays a vital role in various research and industries due to its relatively low price compared to other noble metals.

Recently, noble metal/conducting polymer composites are attracting attention because of their unique structure and potential for use as improved sensors or catalysts. There are various methods of immobilizing a noble metal onto a polymer surface by applying current or voltage to a metal ion interacting with a functional group of the polymer or using chemical reduction. Typically, electrodeposition, ultrasonication, liquid phase reduction using an oxidizing agent, etc. are reported to be widely used [49-55].

1.1.3.2. Metal oxide/carbon composite materials

Metal oxides are chemical compound that consisted of metal, especially cation or transition metal and oxygen. This material is used in diverse applications such as catalysts, supercapacitors, batteries and sensors due to catalytic properties, high surface area to volume ratio, and porosity. Because of this feature, it showed high performance in devices such as sensors and energy device, but redox cycle proceeding during device operation collapses structure which means poor device stability. Also, low conductivity made it difficult to operate gas sensor in room temperature. To overcome these shortcomings, efforts have been made to increase the surface area of metal oxides or to make composites with other materials. Especially, metal oxide/carbon composite materials are promising alternative due to high conductivity and considerable mechanical properties of carbon. In addition, it is easy to combine carbon and metal oxide sources, which has the advantage of simultaneously producing carbon and metal oxide. A typical example is the stabilization of a metal hydroxide / polymer composite in air followed by carbonization at high temperature [56-62].

1.1.4. Electrodeposition

There are various methods for manufacturing composite materials such as auto clave thermal reduction, chemical reduction and electrodeposition. Among them, electrodeposition is highlighted by the ability to coating metal, metal oxide, polymer on substrate with easy thickness, size, and shape control. This method reduces the metal ions in the electrolyte by applying voltage or current to the conductive substrate. Unlike conventionally electrodeposition has used as coatings, various methods such as surface treatment on conductive substrates or addition of other ions in the electrolyte to control the diffusion rate of targeted cation have been studied (**Figure 10**) [63-70].

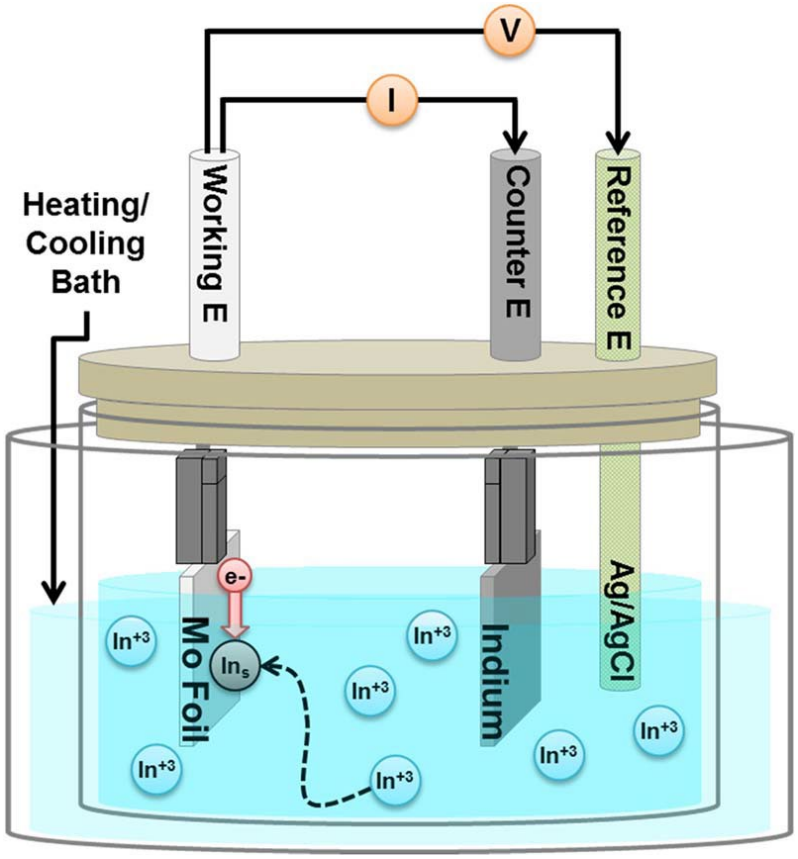

Figure 10. Schematic diagram of electrodeposition [71].

1.1.5. CVD graphene

Graphene, carbon in the form of single or few layer sheets of atom in a two dimensional with sp^2 hybrid carbon, have attracted a great deal of interest from research and industrials application because of their unique physical, mechanical, optical, and electrical properties. There have been diverse methods of graphene fabrication, such as mechanical exfoliation, reduction of graphene oxide, electrochemical or chemical exfoliation of graphite, epitaxial growth [72-73]. However, these methods result in poor quality compared to theoretical properties of graphene. Additionally, preparation of large area graphene was hardly impossible due to described method is top-down process. On the other hands, CVD method facilitated production of large area graphene with high quality. The key step of CVD graphene fabrication is carbon source (mainly hydrocarbon gas) dissolution in metal template such as copper or nickel at high temperature. This dissolved carbon source precipitates in the form of hexagonal ring structure carbon when the metal template is quenched. Therefore, various shapes of graphene can be manufactured according to the sort of metal template (**Figure 11**) [74-77].

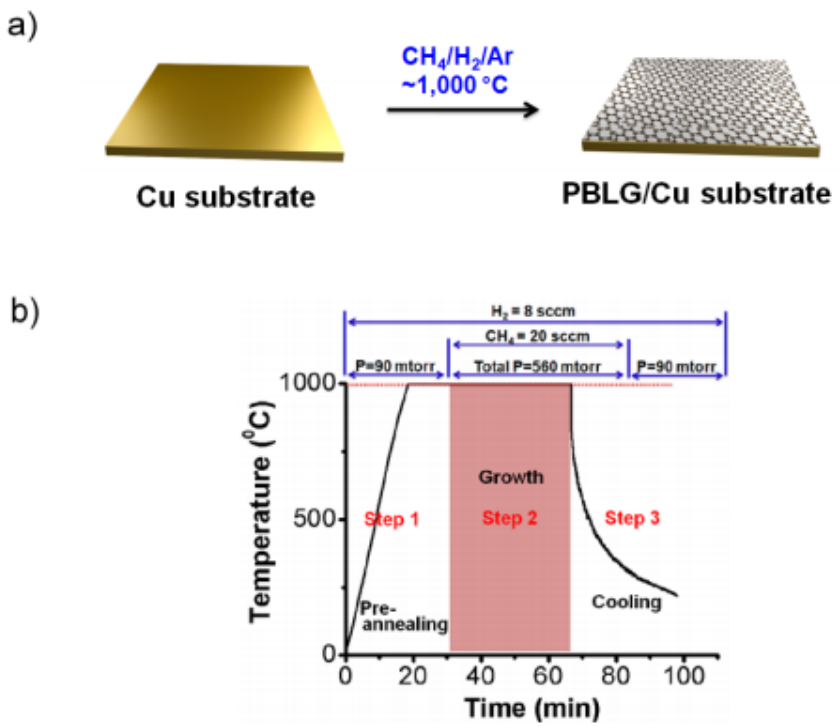

Figure 11. (a) Schematic diagram CVD process, and (b) time dependence of experimental parameter [78].

1.1.6. Sensor application

Sensor is electronic devices, modules, or subsystems that detect changes or stimuli and turn them into identifiable signals. This device consists of an active sensing material and a signal transducer. They react with the target and transmit the signal without distortion (**Figure 12**). Various methods such as high pressure liquid chromatography, gas chromatography coupled with mass spectrometry, and infrared spectroscopy have been used as sensors. However, due to high cost, huge data sampling, expensive, complexity of sample preparation and measurement, and mental maintenance, application of these techniques for real-time sensor is unrealistic. As an alternative, solid state sensors have been used to detect a variety of targets over the last two decades. [79-85].

There are several critical sensor elements for high performance such as sensitivity, selectivity, response/recovery time, working temperature, and stability. In order to satisfy these various factors, nanomaterial is promising candidate for transducer because of their small size, high surface area, and unique electrical properties [86-87].

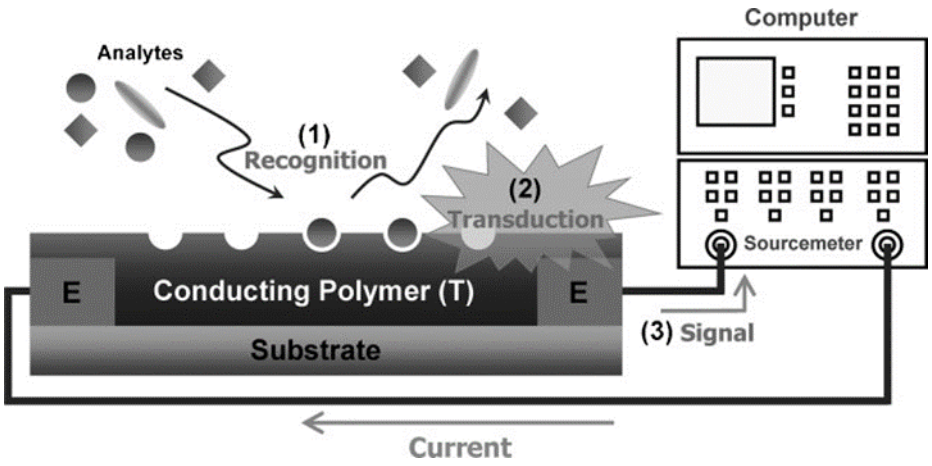

Figure 12. Schematic explanation of sensor mechanism [88].

1.1.6.1. Liquid electrolyte gated FET type sensor.

In order to detect bio-target analytes, the biosensor consists of reaction units such as metal, antibodies, enzymes and aptamers and transducers. Measurement of the target analyte mechanism could be explained by converting signal that arises from analyte-receptor combination to electrical signal that could be analyzable [89-90].

Biosensors can be classified by output signal type for instance, electrical, optical, piezoelectric, fluorescent, and so on. Among various biosensor, FET type biosensor have received considerable attention as desirable candidate due to their current amplification and enhanced signal-to-noise (S/N) ratio (**Figure 13**). In addition, miniaturization, low operating voltage and ultra-low minimum detectable concentration (in femto- and pico- level) are also the reason for attention. This type of sensor composed of metal (e.g. gold, silver) electrode, transducer materials (e.g. conducting polymer, carbon) and target selective receptor [91-96].

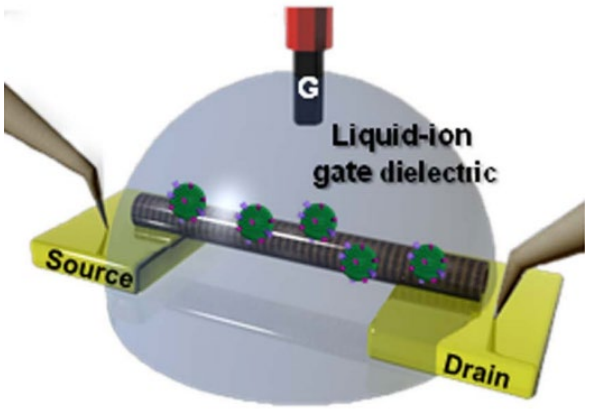

Figure 13. Schematic illustration of liquid-ion gated FET-type sensor [97].

1.1.6.1.1. Hydrogen peroxide (H_2O_2) sensor.

Reactive oxygen species (ROS), including superoxide, hydroxyl radicals, peroxynitrite and hydrogen peroxide could be used as monitoring of biometabolism. In vivo, these molecules are associated with various enzyme systems, including mitochondrial electron transport, cytochrome P450, nicotinamide adenine dinucleotide phosphate (NADPH) complexes and xanthine oxidase. Recently, ROS have been shown to exhibit both protective and toxic effects in a living system. While appropriate concentrations of ROS modulate redox balance, which plays a substantial role in regulating signaling pathways, ROS imbalances are closely associated with various diseases. Especially, abnormally high concentrations of H2O2, for example, are related to neurodegenerative disorders, such as Parkinson's disease and Alzheimer's disease. Additionally, sudden increases in H_2O_2 levels can be related to diabetes and several different types of cancer [98-103].

In, general, the receptor for H_2O_2 sensor was composed of protein such as enzyme. In spite of high selectivity, intrinsic properties of enzyme which is sensitive to pH, temperature, humidity and etc., makes it difficult to use in harsh condition. Therefore, a large effort has been devoted to substitute receptor type such as metal oxide or noble metal.

There high stability and catalytic activity make it and effective alternative to enzyme [104-107].

1.1.6.1.2. Platelet-derived growth factor (PDGF) sensor

Platelet-derived growth factor (PDGF) is protein growth factor that regulate cell growth and division. Particularly, PDGF abnormally high concentration indicates pulmonary hypertension, atherosclerosis, balloon injury-induced restenosis, organ fibrosis, and tumorigenesis [108-109].

The PDGF are composed of two type of monomers: A and B. Therefore, combination of PDGF is PDGF-AA, PDGF-AB, and PDGF-BB. Among them, PDGF-BB is oncogene protein that frequently soar in malignant tumor and is used as a potential cancer marker. Due to this structural complexity, PDGF sensors require particularly high selectivity. Accordingly, oligonucleotide or peptide molecules that bind to specific target analyte, called aptamer, is reasonable candidate for PDGF sensor. The aptamer shows high selectivity so that PDGF-AB and PDGF-BB can be distinguished by normalized signal change [110-112].

1.1.6.2. Chemiresistive sensor

Chemical gas sensor plays critical role in industry or public safety and environmental pollution measurement. Since toxic or dangerous chemical gas is used in biochemical terrorism, the detection technology for those gases is very important. Among various gas sensors, the method of measuring resistance change is very prefer owing to its simple operation, low production cost, miniaturization, and relatively high sensitivity [113].

Typical gas sensors include active materials that are sensitive to the target and gas. when active layer reacts with target molecules, resistance change occurred. This change in resistance is due to changes in the electrical properties of the active layer during the reaction. The electron withdrawing or electron donating action with the target produces a change in resistance depending on what is the main charge carrier of the active layer [114-115].

Traditionally, metal oxide semiconductor has been widely used as active layer for resistive chemical sensors with wide range of detecting molecules such as hydrogen sulfide (H_2S), hydrogen gas (H_2), ammonia (NH_3), nitrogen dioxide (NO_2) and ethanol. However, there is a disadvantage that requires a high operating temperature. To overcome

this problem, research has been conducted for fabricating organic/metal oxide composite is widely studied [116-117].

1.1.6.2.1. DMMP gas sensor.

Toxic and hazardous gases used in warfare and campaign of terror have caused numerous victims with high mortality rates. For example, in 1998, during the massacre of Halavza in Iraq, about 5,000 people were killed using hazard gas mixtures. Organophosphorus compounds such as sarin, tabun, soman, and VX are the main ingredients. Because they are colorless and odorless, they could paralyze human body without visible changes. Therefore, developing of detection technique for organophosphorus gas is one of the most important research area. However, these gases are so lethal that even applying them directly to research is limited. Therefore, dimethyl methylphosphonate (DMMP) gas is used for the experiment because of similar structure and sensing mechanism compare to organophosphorus gases [118-121].

1.1.6.3. Flexible sensors.

Nowadays, there is a growing demand of flexible and portable electronic for various fields such as electronic skin, smart cloth, display, and so on. In line with this trend, researches on sensors based on flexible substrates are also being on the march. Wearable sensing systems have been developed relied on the development of nano-scale materials and the development of various devices. However, there was a limit to their applications as flexible sensors due to rigid materials used in substrate and transducer. Therefore, it is critical to fabricate flexible, and free-standing substrate and transducer. In this manner, various substrates such as Polydimethylsiloxane (PDMS), polyethylene terephthalate (PET), etc. have been widely studied with both scientific and industrial point of view. However, these materials are not conductive and require the addition of a transducer on the substrate. The contact surface generated at this time causes many limitations and problems when manufacturing the device, making it difficult to use as a flexible sensor. Thus, there is a need for a substrate that is flexible, free-standing and conductive at the same time [122-126].

1.2. Objectives and Outlines

1.2.1. Objectives

Aim of this dissertation is providing novel method for fabrication of electrospun polyacrylonitrile nanofibers (PAN NFs) based mats for bio and chemiresistive sensor. In detail, different kinds of post processing such as vapor phase polymerization (VDP), electrodeposition, chemical reduction of metal ion, chemical vapor deposition (CVD), and carbonization were adopted to fabricate flexible and/or free-standing mat. According to the facile synthesis method in each experimental condition, electrospun PAN NFs based mats could be obtained with unique and enhanced properties. These as prepared materials applied to several bio/chemiresistive sensor application such as reactive oxygen species (H_2O_2), growth factor that regulate cell growth and division (PDGF-B), nerve agent simulant (DMMP), respectively

1.2.2. Outlines

The doctoral dissertation involves the following subtopics:

I. Flexible palladium nanoparticle decorated electrospun polypyrrole/ polyacrylonitrile nanofibers of hydrogen peroxide coalescing detection.

II. Copper derived CVD carbon/electrospun-carbon flexible mat for PDGF biosensor.

III. Mn@CNF flexible mat for DMMP gas sensor.

Each subtopic contains experimental details, characterization of fabricated material, and real-rime sensing performance.

2. Experimental Details

2.1. Flexible Palladium nanoparticle decorated electrospun polypyrrole/polyacrylonitrile nanofibers for hydrogen peroxide coalescing detection.

2.1.1. Materials

PAN (Mw = 150 000), pyrrole (98%), iron (III) chloride ($FeCl_3$), palladium (II) chloride ($PdCl_2$), phosphate buffer saline (PBS), hydrogen peroxide solution 30% in H_2O and sulfuric acid (H_2SO_4) were purchased from Aldrich Chemical Co. DMF was purchased from Junsei chemical.

2.1.2. Fabrication of Pd_PPy/PAN NFs

PAN was dissolved in DMF at 70°C for 4 h and PAN NFs were electrospun from the PAN/DMF solution (10 wt%). During electrospinning, the solution was injected through a stainless steel needle connected to a high-voltage power supply (Nano NC, 15 kV) at 10 μl/min. PAN NFs flowed consistently out to the collector. The collected PAN NFs were immersed in a 10 wt% $FeCl_3$ aqueous solution. Fe ion-absorbed PAN NFs were then exposed to a 3-carboxylated pyrrole monomer vapor in vacuum to form PPy/PAN NF films.

The Pd deposition was conducted by electrodeposition method. Electrolyte for electrodeposition was 0.1 M $PdCl_2$ aqueous solution. The morphology of Pd was controlled during electrodeposition by the presence or absence of 0.01 M sulfuric acid in the electrolyte solution. Electrodeposition was carried out in a three-electrode system consisting of the PPy/PAN NF working electrode, a Pt counter electrode, and an Ag/AgCl reference electrode. A constant voltage (-0.1 V) was applied for 10 min to deposit Pd nanoparticles.

2.1.3. Electrical measurement of Pd_PPy/PAN NFs based non-enzyme sensor

All electrical measurements were conducted with a keithley 2612 sourcemeter, probe station (MS TECH, Model 4000) and an automatic battery cycler (Wonatech WBCS 3000). To construct FET sensor configuration, silver paste was deposited on the edge of Pd_PPy/PAN NFs. In addition, a solution chamber (volume: 200 μL) was designed and used to facilitate the solution-based measurement. The change of the current was normalized by following equation.

$$S = \left[\frac{\Delta I}{I_0}\right]_{SD} (\%) = \frac{(I - I_0)}{I_0}$$

S: sensitivity

I: measured real-time current

I_0: initial resistance

2.1.4. Characterization

Field-emission scanning electron microscope (FE-SEM) micrographs were obtained with a JEOL 6700 instrument. JEOL JEM-200CX and -3010 instruments were used to acquire transmission electron microscopy (TEM) and high-resolution TEM (HR-TEM) micrographs, respectively. X-ray photoemission spectroscopy (XPS) and X-ray diffraction (XRD) experiments were performed on JPS-9000MS (JEOL; Mg Kα X-ray source) and M18XHF-SRA (Rigaku SmartLab; λ = 1.5418Å) instruments, respectively. Raman spectra were acquired on an FRA 1106/S FT-Raman (Bruker) spectrometer and excited with a 514-nm Ar laser.

2.2. Copper derived CVD carbon/electrospun-carbon flexible and free-standing mat for PDGF biosensor.

2.2.1. Materials

PAN (M_w = 150,000), PDGF-AA, PDGF-AB, PDGF-BB, calmodulin (Cal.), adenosine triphosphate (ATP) and bovine serum albumin (BSA) were purchased from Aldrich Chemical Co. The PDGF-B binding aptamer was purchased from Bioneer Co. (Dajeon, Korea) and modified at the 5-terminus with an amine group (5`$NH_2$ CAG GCT ACGGCA CGT AGA GCA TCA CCA TGA TCC TG3`). N,N-dimethyl formamide (DMF) was purchased from Junsei chemical. Spherical and flaky Cu powder were purchased from Join M (Nonsan, Korea)

2.2.2. Fabrication of CuC/CNF mat

PAN was dissolved in DMF at 70 °C for 4 h and PAN NFs were electrospun from the PAN/DMF solution (13 wt%). During electrospinning, the solution was injected through a stainless steel needle connected to a high-voltage power supply (Nano NC, 10 kV) at 5 μl/min. The electrospun PAN NFs were heated to 270 ℃ with a constant heating rate of 1 ℃ min^{-1} and stabilized for 1 h in ambient air.

Two types of Cu powder (spherical and flaky) were coated on stabilized PAN NFs. Cu powder coated NFs were located in the chamber and heated to 1000 ℃ at 147 mTorr (H_2) and flow rate of 8 sccm. This condition was held for 30 min to eliminate the copper oxide layer and stabilize the chamber atmosphere. Then, methane (CH_4) gas used as a carbon source was fed at a flow rate of 20 sccm for 30 min. Thereafter, the furnace chamber was cooled at 40 °C min^{-1} to room temperature. The CuC/C mat were acquired by etching Cu powder and rinsed with deionized water several times.

2.2.3. Electrical measurement of CuC/CNF mat aptamer sensor

All electrical measurements were conducted with a keithley 2612 sourcemeter, probe station (MS TECH, Model 4000) and an automatic battery cycler (Wonatech WBCS 3000). To construct FET sensor configuration, silver paste was pasted on the both end of CuC/C mat. In addition, a solution chamber (volume: 200 μL) was designed and used to facilitate the solution-based measurement. The change of the current was normalized by following equation.

$$S = \left[\frac{\Delta I}{I_0}\right]_{SD} (\%) = \frac{(I - I_0)}{I_0}$$

S: sensitivity

I: measured real-time current

I_0: initial resistance

2.2.4. Characterization

FE-SEM micrographs were obtained with a JEOL 6700 instrument. JEOL JEM-200CX were used to acquire TEM micrographs XPS and XRD experiments were performed on JPS-9000MS (JEOL; Mg Kα X-ray source) and M18XHF-SRA (Rigaku SmartLab; λ = 1.5418Å) instruments, respectively. Raman spectra were acquired on an FRA 1106/S FT-Raman (Bruker) spectrometer and excited with a 514-nm Ar laser. The two-probe method was used to measure the resistance changes according to the number of bending test.

2.3. Mn@CNF flexible and free-standing mat for DMMP gas sensor.

2.3.1. Materials

PAN (M_w = 150 000), pyrrole (98%), ammonium perchlorate (APS), potassium permanganate ($KMnO_4$), acetone, benzene, chloroform, ethanol, hexane, toluene and dimethyl methylphosphonate were purchased from Aldrich Chemical Co. DMF was purchased from Junsei chemical. 4-(4,6-Dimethoxy-1,3,5-triazin-2-yl)-4-methyl morpholinium chloride (DMT-MM) were purchased from Fluka (Buchs, Switzerland).

2.3.2. Fabrication of Mn@CNF mat

PAN was dissolved in DMF at 70 °C for 4 h and PAN NFs were electrospun from the PAN/DMF solution (13 wt%). During electrospinning, the solution was injected through a stainless steel needle connected to a high-voltage power supply (Nano NC, 10 kV) at 5 μl/min. The electrospun PAN NFs were sock in APS 3% aqueous solution. APS socked PAN NFs were then exposed to pyrrole monomer vapor at 60 ℃ and rinsed several times to form PPy/PAN NFs. The PPy/PAN NFs were then immersed in 0.01 M $KMnO_4$ aqueous solution and heated for 30 min. After washed several times, $KMnO_4$ treated PPy/PAN NFs were stabilized at 270 ℃ and carbonized at 700℃ to make Mn@CNF mat.

2.3.3. Electrical measurement of Mn@CNF mat chemiresistive gas sensor

Gas sensor electrode was fabricated by painting silver paste to both edge of Mn@CNF mat. The electrode was set in the chamber and connected to source meter to monitor the electrical change. In this experiment, VOC dissolved in water was vaporized by using bubbler and diluted with N_2 gas. Then, sensor electrode was exposed to diverse concentration of vaporized and diluted target gases and non-target gases. The sensor performance was calculated by measuring the normalized electrical resistance change with applying constant current (10^{-6} A) to the electrode. The normalized resistance change was defined by following equation.

$$S = \frac{\Delta R}{R_0} = \frac{(R - R_0)}{R_0}$$

S: sensitivity

R: real-time resistance

R_0: initial resistance

After the sensor electrode had been exposed to VOC gases for enough time, VOC gases were purged with inert gas to recover the conductance. In addition, response and recovery time were defined as the time required

for a sensor to reach 90% of maximum sensitivity after fed VOC gases and the time required for a sensor to reach 10% of the preceding sensitivity after purging inert gas, respectively.

2.3.4. Characterization

FE-SEM micrographs and EDX spectra were obtained with a JEOL 6700 instrument. JEOL JEM-200CX were used to acquire TEM micrographs. XPS and XRD experiments were performed on JPS-9000MS (JEOL; Mg Kα X-ray source) and M18XHF-SRA (Rigaku SmartLab; λ = 1.5418Å) instruments, respectively. Raman spectra were acquired on an FRA 1106/S FT-Raman (Bruker) spectrometer and excited with a 514-nm Ar laser. The two-probe method was used to measure the resistance changes according to the number of bending test.

3. Results and Discussion

3.1 Flexible Palladium nanoparticle decorated electrospun polypyrrole/polyacrylonitrile nanofibers for hydrogen peroxide coalescing detection.

3.1.1. Fabrication of the Pd_PPy/PAN NFs

Figure 14 shows the overall process used to fabricate the shape-controlled palladium nanoflower decorated polypyrrole/polyacrylonitrile nanofibers (Pd_PPy/PAN NFs). First, a polyacrylonitrile (PAN) solution was electrospun onto the collector at a constant voltage, resulting in *ca.*180 nm polyacrylonitrile nanofibers (PAN NFs) (**Figure 15a and b**) [127]. The electrospun PAN NFs were soaked in a solution of 10 wt% $FeCl_3$, resulting in the adsorption of iron (Fe) cations onto the PAN NFs surface *via* charge-charge interactions between Fe^{3+} ions and the partial negative charge of nitrogen atoms in the PAN. To coat with PPy, the Fe-adsorbed PAN NFs were exposed to pyrrole monomer vapor at room temperature in a vacuum system. Polymerization occurred at the PAN NFs surface, facilitated by the adsorbed Fe^{3+} ions. Uniformly adsorbed Fe^{3+} resulted in homogeneous, aggregate-free polypyrrole (PPy) coatings with a thickness of *ca.* 10 nm (**Figure 15c and d**).

The PPy/PAN NFs were then decorated with shape-controlled Pd nanoparticles *via* electrodeposition. The PPy/PAN NFs were used as the working electrode, silver/silver chloride (Ag/AgCl) as the reference electrode, and Pt wire as the counter electrode. The three electrodes were immersed in an aqueous solution of $PdCl_2$. The Pd^{2+} ions preferentially approached the surface of the PPy by charge-charge interactions with carboxyl groups on the PPy surface. With the application of a constant voltage, Pd^{2+} ions in the vicinity of the PPy surface were reduced, forming Pd nanoparticles [128]. The shape of the nanoparticles was influenced by the presence of 0.01 M sulfuric acid in the electrolyte solution. In the absence of sulfuric acid, the Pd nanoparticles exhibited blunt, rounded edges (**Figure 16a**), whereas sharp features were formed in the presence of sulfuric acid (**Figure 16b**). As a result, two shapes of Pd nanoparticles were embedded on the PPy surface: blunt Pd nanoparticles refer to BPd and sharp Pd nanoparticles named SPd. To confirm the role of sulfate ion (SO_4^{2-}), three diffrent types of Pd nanoparticles were embedded on the surface of PPy with varying the concentration of sulfuric acid in the electrolyte (**Figure 17**). In the growth process of Pd nanoparticles, sulfate ion (SO_4^{2-}) therotically

interferes with particle growth. In particular, this effect is maximized in the (111) plane of the Pd which has high affinity with SO_4^{2-}. Since the spherical shape of Pd nanoparticle is dominated by (111) plane, the presence of SO_4^{2-} in the electrolyte caused the nanoparticle to grow to a sharp shape. Nevertheless, (200) and (220) planes are also influenced by SO_4^{2-} at high sulfuric acid concentrations, which leads to different Pd morphologies [129-130]. TEM images of the SPd_PPy/PAN NF films showed that the SPds were *ca.* 200 nm in size and embedded in the PPy film, rather than being attached to the film surface (**Figure 16c** and **18**). High-resolution transmission electron microscope (HR-TEM) images of SPds indicate interplanar spacing of 0.224 and 0.195 nm for the (111) and (200) planes, respectively, corresponding to face-centered-cubic (fcc) Pd (**Figure 16d)**.

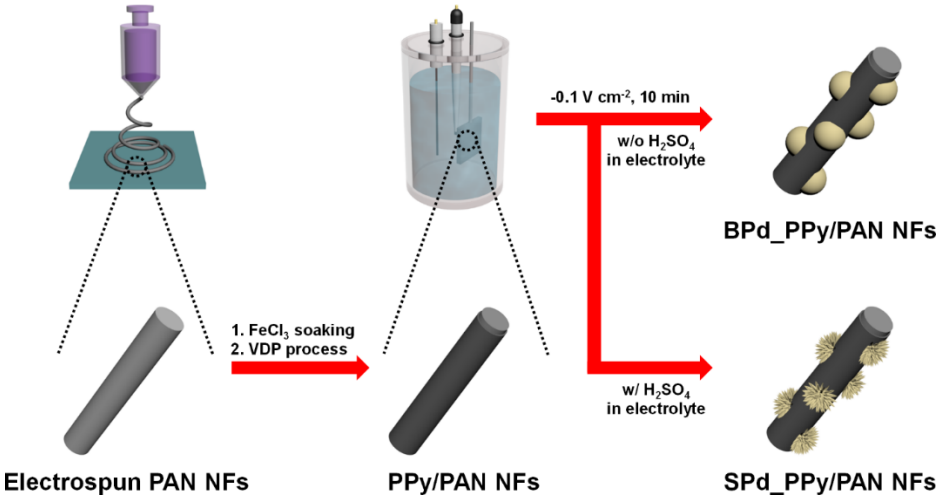

Figure 14. The sequential fabrication Pd_PPy/PAN NFs is shown. The process comprises electrospinning, vapor deposition polymerization and three-electrode system-based electrodeposition with (w/) or without (w/o) sulfuric acid (H_2SO_4) in the electrolyte solution.

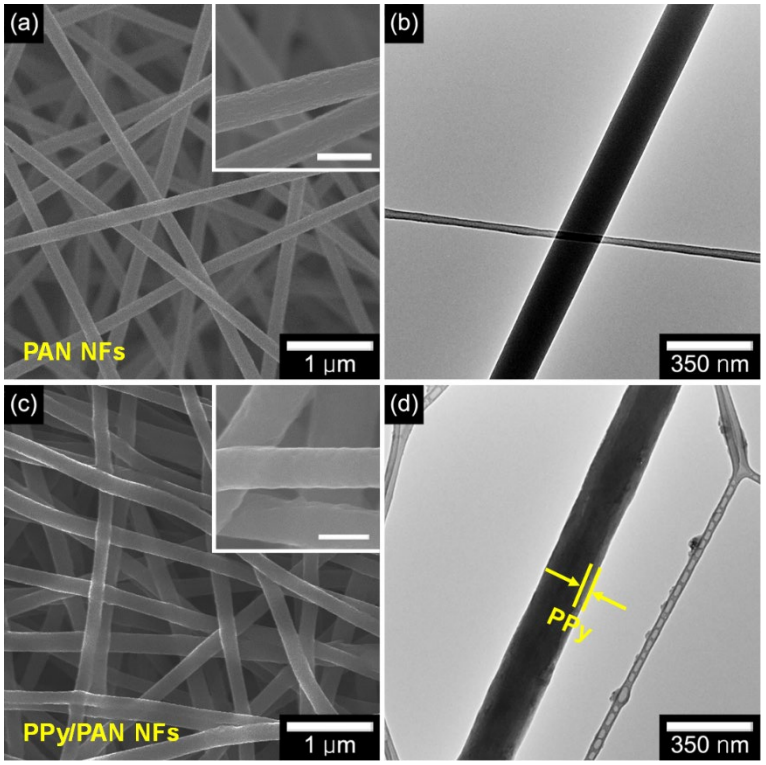

Figure 15. Low- and high-magnification (inset) field-emission scanning electron microscope (FE-SEM) images of (a) PAN NFs, (b) Transmission electron microscope (TEM) image of PAN NFs, (c) Low- and high-magnification (inset) of FE-SEM images of PPy/PAN NFs and (d) TEM images of PPy/PAN NFs, respectively (scale bar of inset: 200 nm).

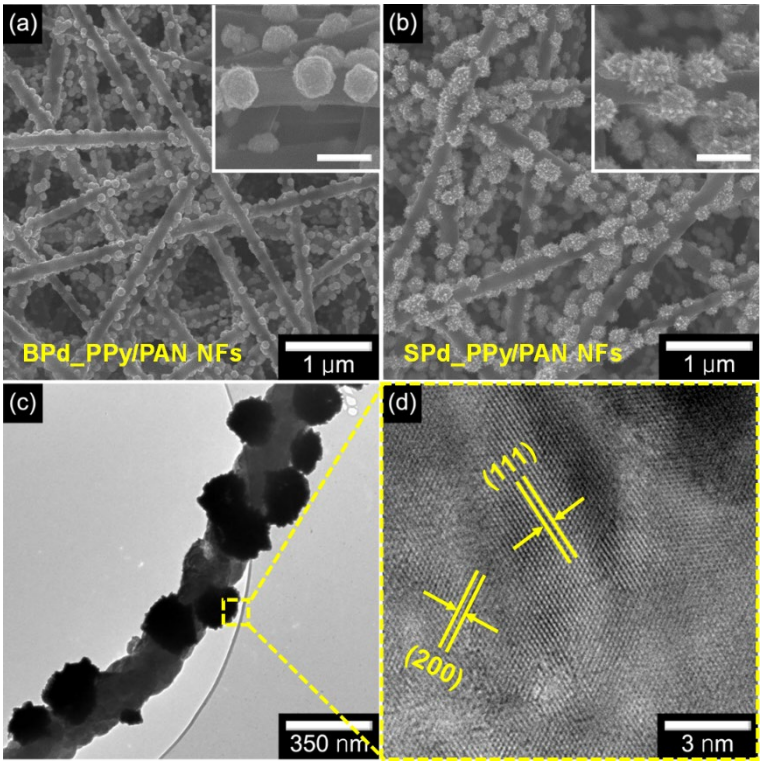

Figure 16. FE-SEM images of (a) BPd_PPy/PAN NFs, (b) SPd_PPy/PAN NFs, respectively (scale bar of inset: 200 nm). (c) TEM images of SPd_PPy/PAN NFs, and (d) HR-TEM micrographs of SPd_PPy/PAN NFs.

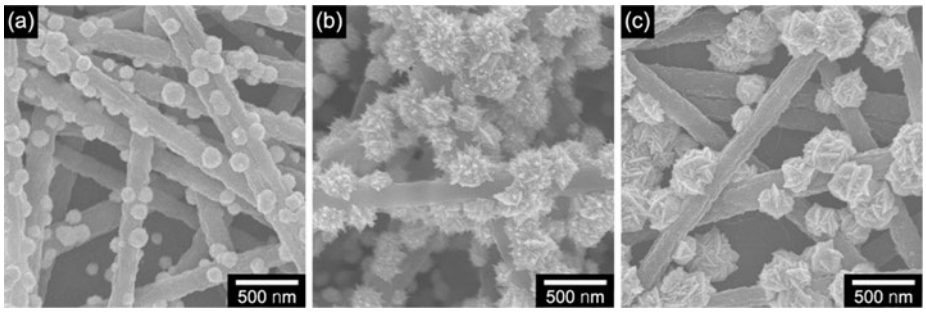

Figure 17. FE-SEM images of Pd_PPy/PAN NFs using (a) absence (b) 0.01 M (c) 0.1 M of sulfuric acid as electrolyte.

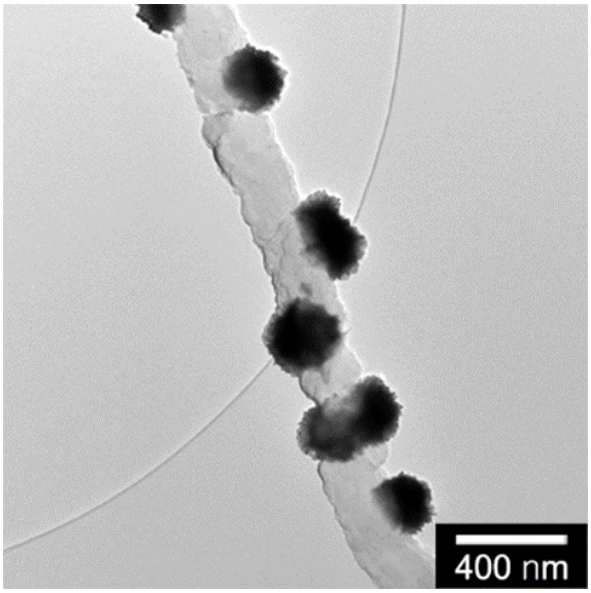

Figure 18. TEM images of SPd_PPy/PAN NFs with over focusing.

3.1.2. Characterization of the Pd_PPy/PAN NFs

Powder X-ray diffraction (XRD) patterns provided additional information about the structural development at each fabrication step (**Figure 19a**). The electrospun PAN NFs showed a characteristic diffraction band at the 2θ angle of 16.8°, corresponding to the orthorhombic (110) reflection. Despite the VDP or deposition process, presence of these strong band in other sample indicated conservation of the PAN structure. The broad peak at 23° was enhanced due to the amorphous PPy structure, and resulted from scattering by the PPy chains at the interplanar spacing. The diffraction peaks at 2θ = 40.12° for (111) plane, 46.3° for (200) plane, 67.8° for (220) plane and 81.6° for (311) plane matched well with the fcc lattice of Pd, indicating that the Pd was successfully reduced by electrons during the electrodeposition process [131]. **Figure 19b** indicates the Raman spectra ranging from 1,000 to 2,000 cm^{-1}. The D band typically represents disordered graphite, while the G band is attributed to the in-plane displacement of carbon atoms in the aromatic structure. Therefore, the I_D/I_G ratio (the intensity ratio between D and G bands) facilitates the determination of the degree of graphitization. The two characteristic D and G peaks observed for the PPy/PAN NFs corresponded to stretching of the π-conjugated structure

and the ring stretching mode of PPy, whereas the PAN NFs spectrum only displays the nearly featureless. The I_D/I_G ratio of the SPd_PPy/PAN NFs was higher than that of the PPy/PAN NFs, which implied that the decoration of Pd within the PPy decreased the degree of graphitization [132-133]. The chemical composition was investigated using XPS The wide-scan XPS spectra over the range of 0 to 1,200 eV, demonstrated the presence of Pd in the SPd_PPy/PAN NFs (**Figure 19c**). Furthermore, the high-resolution XPS spectrum of the Pd peaks revealed $3d_{5/2}$ and $3d_{3/2}$ spin-orbit components (observed near 335 and 341 eV, respectively), which indicated that the valence state of Pd was Pd^0 (**Figure 19d**) [134]. In addition, the presence of carboxyl groups in the SPd_PPy/PAN NFs was revealed by O 1s XPS spectra (**Figure 20**).

Repeated bending experiments were conducted to determine the flexibility of the materials. **Figures 21a and 21b** display the flat or bent condition of SPd_PPy / PAN NFs, respectively. Despite 300 times of repetitions, the electrical resistance increased by only 13.37%. Considering the above result, SPd_PPy/PAN NFs could be thought flexible. (**Figure 22**). However, in the absence of a substrate such as a PEN film that serves as a support, SPd_PPy/PAN NFs are too thin to

maintain flexible properties. Therefore, there is a need for improvements that allow for free-standing and flexibility at the same time.

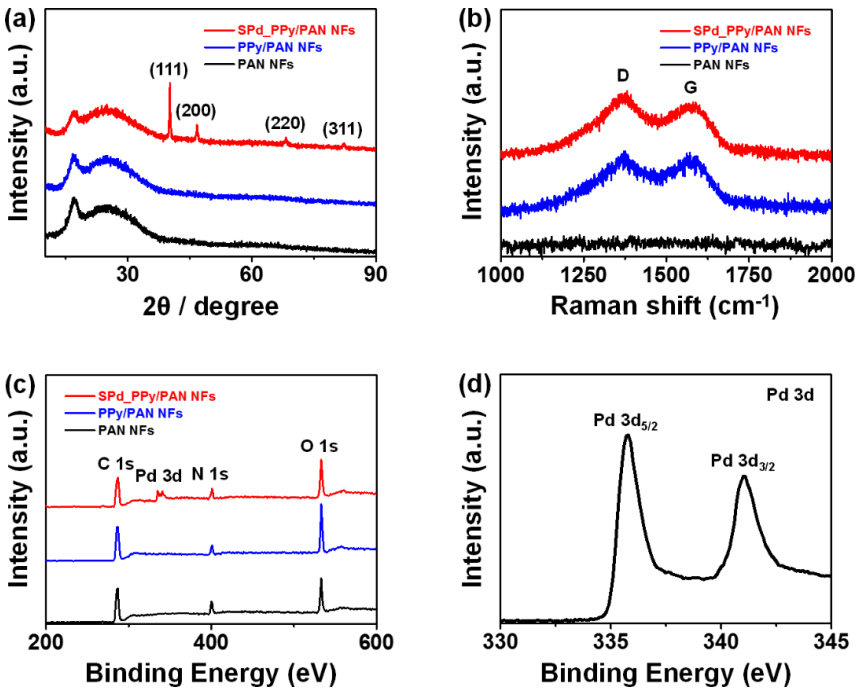

Figure 19. (a) X-ray diffraction (XRD), (b) Raman, and (c) X-ray photoelectron spectroscopy (XPS) data acquired on PAN NFs (black), PPy/PAN NFs (blue) and SPd_PPy/PAN NFs (red). (d) High-resolution XPS of Pd (3d) for SPd_PPy/PAN NFs.

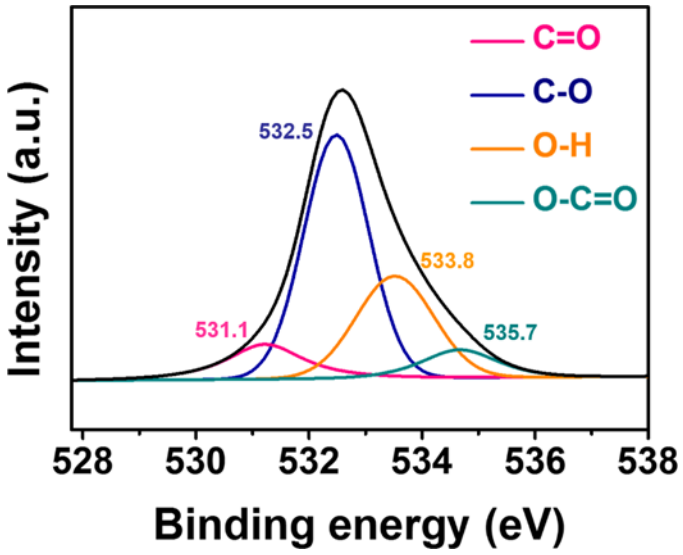

Figure 20. C 1s XPS spectra of SPd_PPy/PAN NFs.

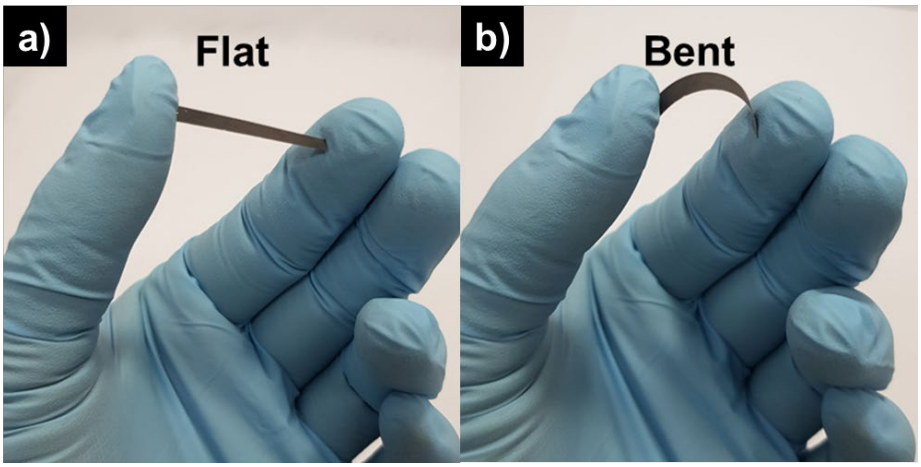

Figure 20. (a) Flat, and (b) bent SPd_PPy/PAN NFs.

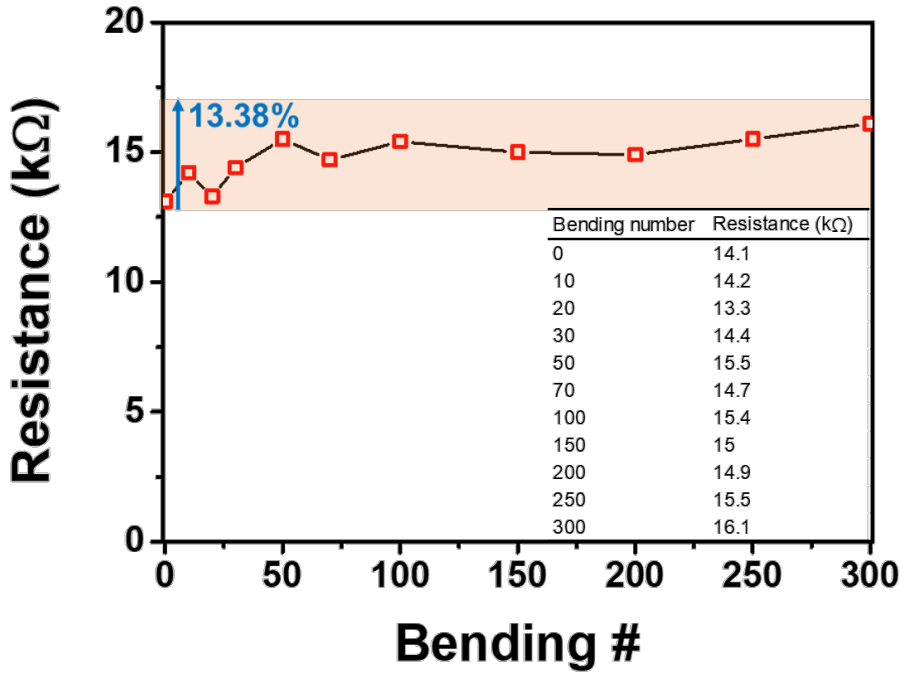

Figure 22. Resistance change of SPd_PPy/PAN NFs with repetitive bending.

3.1.3. Electrical properties of the shape controlled Pd_PPy/PAN NFs electrode.

Current-voltage (*I-V*) curves of the PPy/PAN NF and Pd_PPy/PAN NF films (**Figure 23a**) were measured by applying a liquid-ion-gate voltage (V_G). The Pd_PPy/PAN NF-based electrodes yielded linear *I-V* curves ranging from -0.1 to +0.1 V, indicating ohmic contact. Furthermore, the conductivity (dI/dV) of the Pd_PPy/PAN NFs was higher than that of PPy/PAN NFs due to the high conductivity of metallic Pd.

Figure 23b shows the I_{SD}-V_{SD} curves of Pd_PPy/PAN NF films, acquired at -0.1 V intervals of V_G at a constant scan rate (of 10 mV s^{-1}). The I_{SD} decreased with decreasing V_G due to the p-type behavior of PPy as the charge transfer channel in the field-effect transistor (FET) type system.

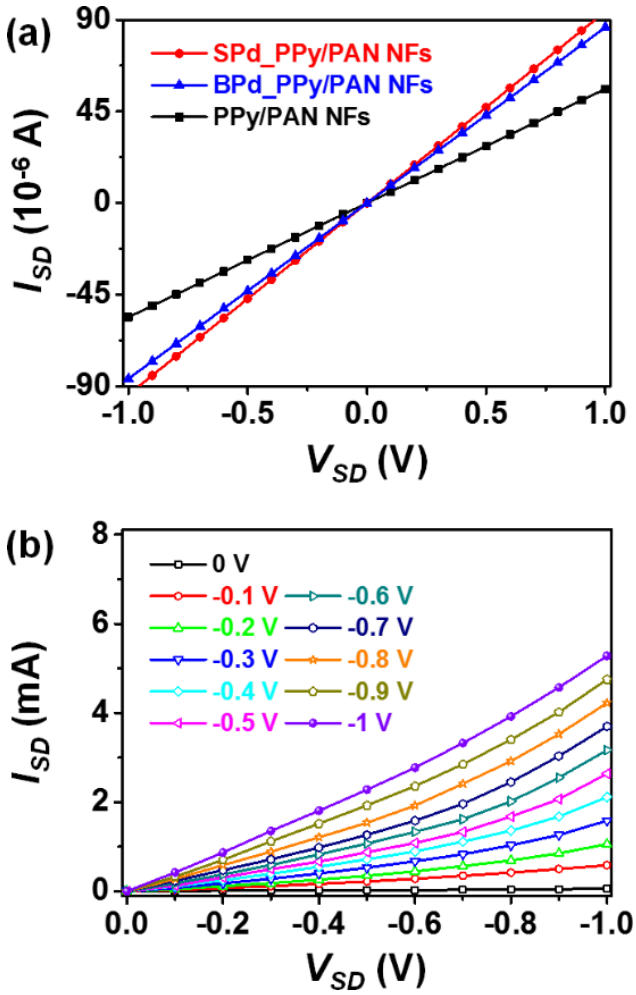

Figure 23. (a) Source-drain current versus source-drain voltage (I_{SD}-V_{SD}) for PPy NFs (black), BPd_PPy/PAN NFs (blue) and SPd_PPy/PAN NFs (red), respectively. (b) I_{SD}-V_{SD} characteristics of SPd_PPy/PAN NF-based liquid-ion-gated FET sensors as a function of gate voltage (V_G) from 0 to -1 V in steps of -0.1 V (scan rate of V_{SD}: 10 mV s^{-1}).

3.1.4. Real-time response of FET-type H_2O_2 sensor based on shape-controlled Pd_PPy/PAN NFs electrode

The I_{SD} was monitored to determine the sensing properties of liquid-ion-gated Pd_PPy/PAN NF-based FET-type films, which consisted of source (S), drain (D) and gate electrodes at a constant V_G of -100 mV and V_{SD} of 1 mV. The sensing mechanism of the Pd_PPy/PAN NFs is displayed in **Figure 24**. The H_2O_2 was doubly oxidized by the catalytic effect of Pd. These two electrons transferred to the top-gate voltage, which became more negative. Consequently, the hole density in the charge transfer pathway of the PPy/PAN NF film increased, leading to an increase in current (I_{SD}). Moreover, H_2O_2 also increased the degree of oxidation ($[N^+]/[N]$ ratio) in PPy, resulting in an increase in the number of holes in the PPy backbone and a further increase in I_{SD} [135] [136].

To investigate the sensing properties of the liquid-ion-gated SPd_PPy/PAN NF-based FET-type sensors, the I_{SD} was monitored in real time during the addition of H_2O_2 to the system at a V_G of -0.1 V (V_{SD} = 1 mV) and a low operating voltage **Figure 25a** presents the real-time response of the PPy/PAN NFs, BPd_PPy/PAN NFs, and SPd_PPy/PAN NFs as a function of H_2O_2 concentration. The I_{SD} rapidly increased with the addition of H_2O_2, reaching saturation within 1 s. Although the

detection limit of the PPy/PAN NF films for H_2O_2 was high (1 mM), the I_{SD} increased slightly due to increasing hole density in the PPy film, as discussed above. The sensitivity of the SPd_PPy/PAN NFs was higher than that of the BPd_PPy/PAN NFs. This likely resulted from the higher catalytic surface area of the SPd nanoparticles, which attained a detection limit of 1 nM at room temperature. The pointed and sharp edges of the SPd particles with numerous active sites for H_2O_2 oxidation facilitated the high sensitivity and low detection limit. **Figure 25b** shows the system sensitivity as a function of H_2O_2 concentration. Sensitivity (S) was defined by the saturation point of the normalized current change ($(\Delta I/I_0)_{SD} \times 100$) measured 10 s after the addition of H_2O_2. At low concentrations (< 100 nM), the Pd_PPy/PAN NF-based FET-type sensors demonstrated nonlinear changes. In contrast, linear behavior was observed over a wide concentration range ($1 – 10^4$ nM).

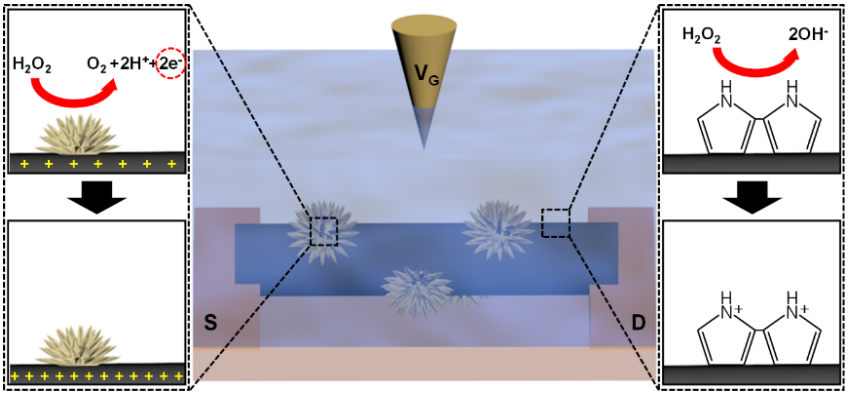

Figure 24. H_2O_2 detection mechanism of SPd_PPy/PAN NFs on an SPd-decorated surface (left) and a PPy surface (right).

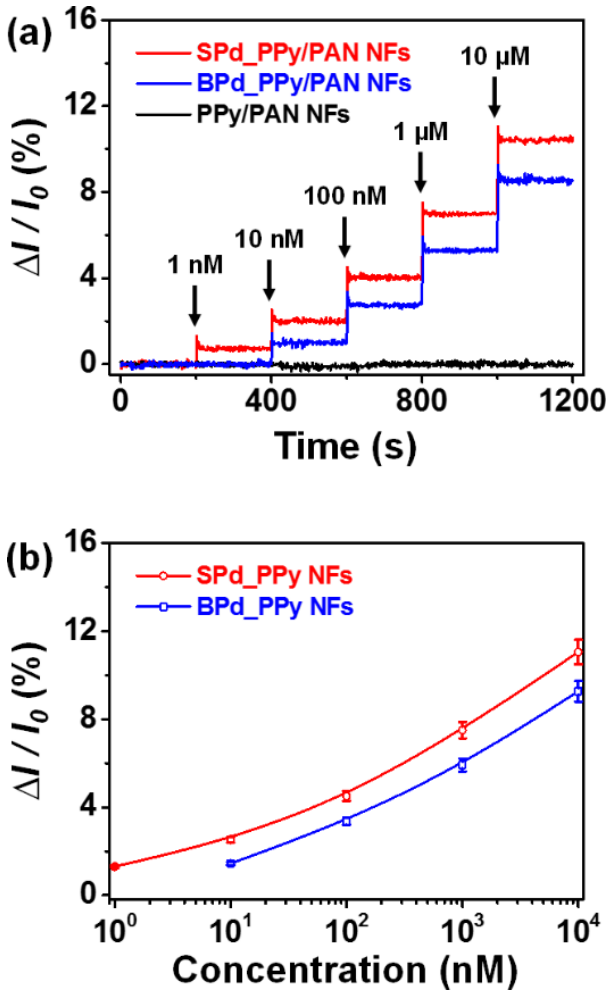

Figure 25. (a) Real-time response of an FET-type sensor with normalized current changes ($\Delta I/I_0 = (I-I_0)/I_0$, where I_0 is the initial current and I is the immediate current). (b) Calibration curves of current changes as a function of glucose concentration (PPy/PAN NFs (black); BPd_PPy/PAN NFs (blue); SPd_PPy/PAN NFs (red)).

3.2 Copper derived CVD carbon/electrospun-carbon flexible and free-standing mat for PDGF biosensor.

3.2.1. Fabrication of the Cu derived carbon/CNF mat.

Figure 1 shows the sequential steps for fabricating Cu derived carbon/CNF mat. As a starting materials, PAN NFs were prepared *via* electrospinning of PAN 13% DMF solution. The electrospun PAN NFs were then heated from 25 ℃ to 270 ℃ with 1 ℃ min^{-1} ramping rate and maintained 1h in air for stabilization. The stabilization aided to convert the branched backbone structures of polyacrylonitrile into ring structure which enhance the crystallinity and mechanical properties. The stabilized PAN NFs were daubed with two type of copper (Cu) powder (flaky and spherical) to form Cu powder/stabilized PAN NFs. The flake type Cu have an average size of 2 to 3 μm in the form of a plate and the sphere type Cu have an average diameter of 1 μm in the form of a sphere, as described in **Figure 27a and b**. The size of the flake type ranged from 0.1 to 8 μm, whereas the size of the sphere type ranged from 0.1 to 3 μm that relatively uniform. Cu powder/stabilized PAN NFs were transformed to Cu derived carbon/CNF (CuC/CNF) through a typical CVD graphene fabrication process. During CVD process, H_2 gas acted

as carrier gas and CH_4 is carbon source that dissolved in Cu. The CH_4 dissolved in copper at high temperatures precipitates to the surface during quenching and forms graphene. Subsequently, carbon-only materials were obtained by removing Cu with Cu etchant. According to the Cu type used, there are two kinds of CuC/CNF: the materials prepared based on the Flake type and sphere type were denoted as FlakeC/CNF and SP10C/CNF, respectively. The FE-SEM images in **Figure 27c and d** exhibit the distinct morphology of FlakeC/CNF (fiber thickness of *ca.* 370 mm) and SP10C/CNF (thickness of *ca.* 400 mm). In the case of using flake type Cu, additional carbon in the form of a net connecting fiber to fiber was fabricated. On the other hand, when sphere type Cu was used as a template for additional carbon, sharp protrusions were added to surface of CNFs. The process of generating protrusions is as follows: first, rounded protrusions are formed on the Cu spheres during the CVD process at high temperature. In the quenching process, then, graphene was formed on the rounded protrusion surface. After the Cu etching process, inside of both sphere and rounded protrusion became emptied. Unable to maintain hollow structure without template, morphology of round protrusion has changed with sharp in tandem with the sphere carbon layer wraps CNF [137-138].

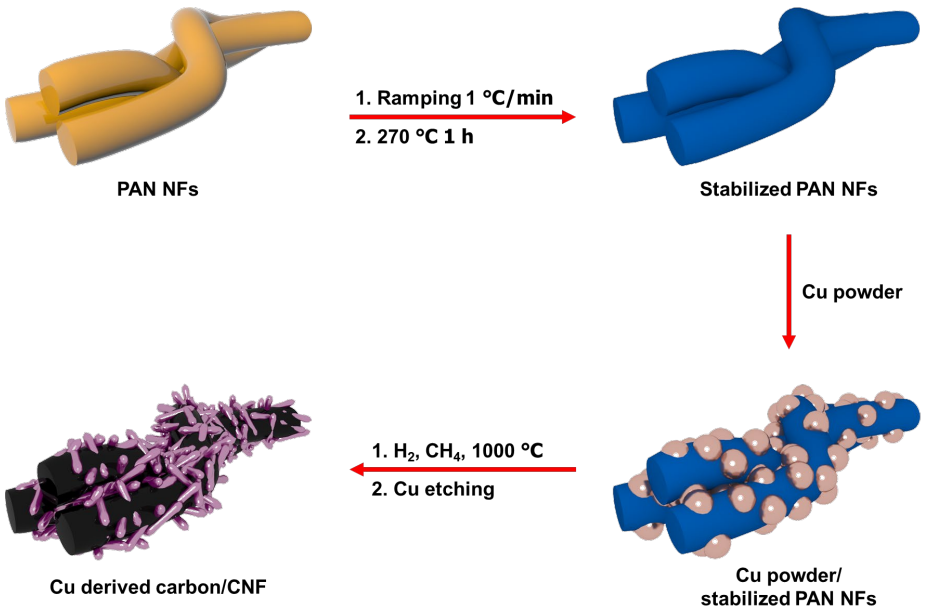

Figure 26. Schematic illustration of sequential steps for fabricating Cu derived carbon/CNF *via* stabilization and CVD process.

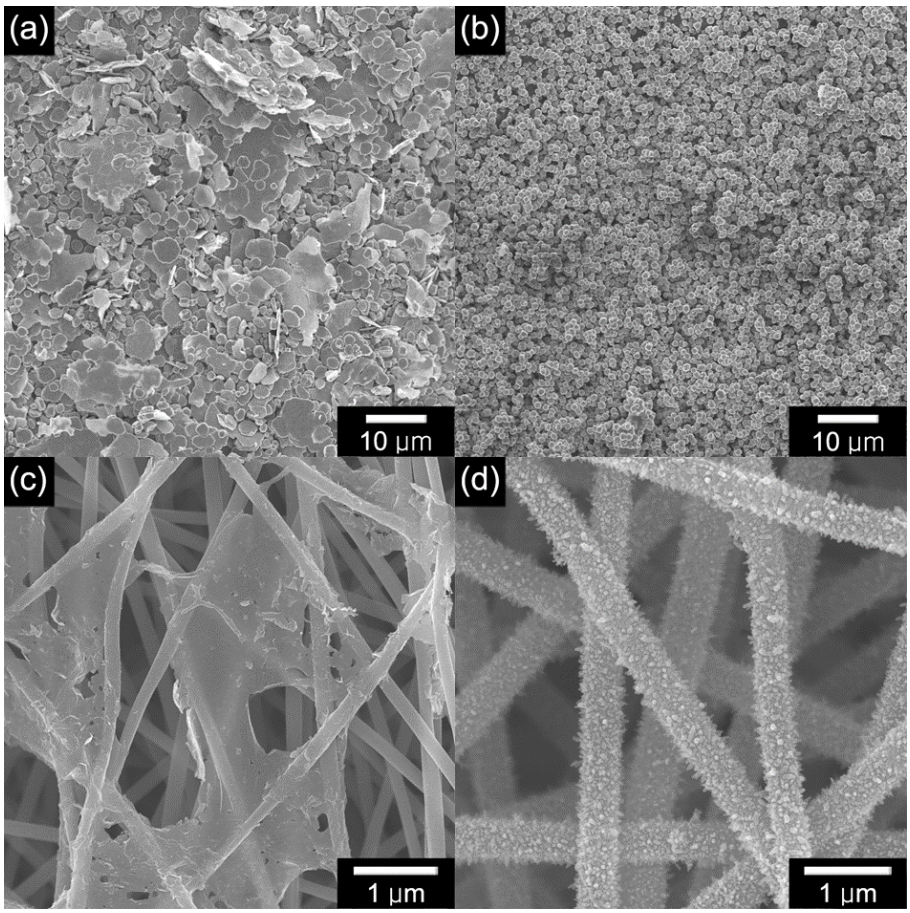

Figure 27. FE-SEM images of (a) flake type copper (Cu) powder, (b) sphere type Cu powder, (c) FlakeC/CNF, and (d) SP/CNF.

3.2.1. Characterization of the Cu derived carbon/CNF mat.

Figure 28 depicts the FE-SEM images and energy-dispersive X-ray spectroscopy (EDX) element dot mapping analysis. Element mapping clearly confirm presence of C, N, and O atom at the SP10C/CNF. The uniformly distributed C mapping shows that the carbon is well formed and the structure does not collapse. In addition, the presence of a significant amount of O atoms, it can be seen that there is a functional group containing O atoms such as hydroxyl group, carboxyl group on the surface of SP10C/CNF. Though, Cu atom mapping and element composition indicate the presence of Cu, but the amount is negligible, which means that Cu removal *via* etchant was successfully conducted. Furthermore, XRD analysis was performed to confirm the Cu removal (**Figure 29**). Both flake and sphere type Cu exhibit characteristic diffraction peaks of Cu. The peaks at 2θ angle of 43.315°, 50.455°, and 74.145° for flake type Cu, and 43.365°, 50.495°, and 74.185° for sphere type cu were corresponding to the (111), (200), and (220). Comparing the spectra of FlakeC/CNF and SP10C/CNF with the corresponding Cu spectra, it can be seen that there are no characteristic peaks of Cu. Moreover, graphite structure of FlakeC/CNF and SP10C/CNF were demonstrated by strong wide band at 2θ of 24.6° and weak band at 2θ of

43.1° which were corresponded to the diffraction of (002) and (100) plane, respectively [139-141].

To achieve an in-depth insight into the properties of fabricated Cu derived carbon, Raman spectra was used. Carbon nanofibers (CNFs) were prepared through the same process except for the Cu coating to utilize as a control. **Figure 30a** indicates the raman spectra of CNF (black) and Flake/CNF (red). Both exhibit D (1338.9 cm^{-1}) and G (1581.3 cm^{-1}) band which are characteristic band for carbon materials. For FlakeC/CNF, 2D band (2657 cm^{-1}) exsisted due to the E_{2g} symmetry mode and second order two-phonon vibration of sp2 hexagonal with diminished I_D/I_G ratio (CNF: 1.147 and FlakeC/CNF: 0.935) than that of CNF. Based on 2D peak and decreased I_D/I_G ratio, the net connecting FlakeC / CNF fibers is called graphene. Similar trends were observed in the raman spectra of CNF and SP10C/CNF (**Figure 30b**). The SP10C/CNF displayed more reduced I_D/I_G ratio (CNF: 1.127 and SP10C/CNF: 0.988) than CNF and 2D peak. Through this, it was confirmed that the protrusion of the fibers surface is graphene in SP10C/CNF. Additionallly, TEM image of SP10C/CNF further testified the above explanation (**Figure 31**). [142-145].

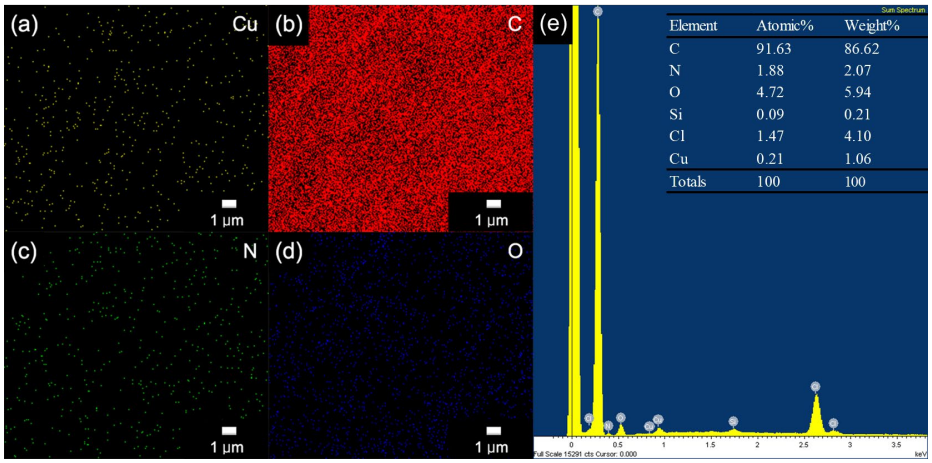

Figure 28. EDX elemental mapping of (a) Cu, (b) C, (c) N, (d) O images. (e) Spectrum investigated for atomic composition and their corresponding atomic and weight percentage.

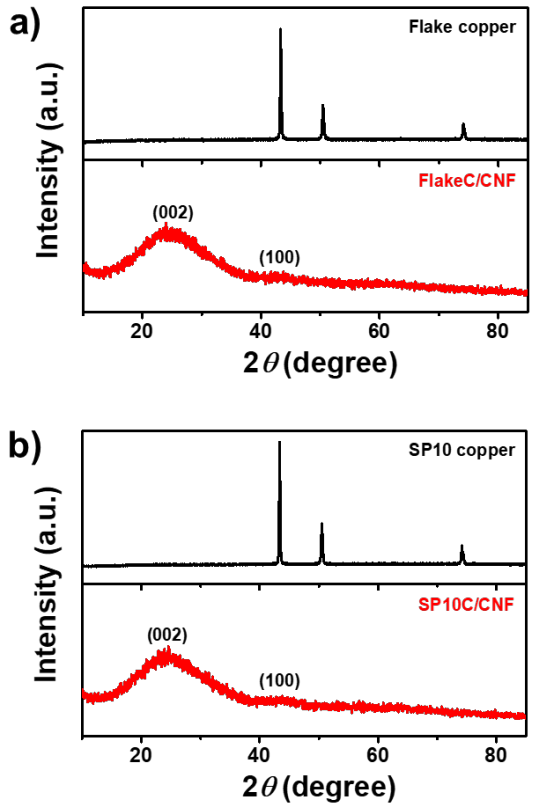

Figure 29. XRD spectra of (a) flake type Cu (black), and FlakeC/CNF (red) and (b) sphere type Cu (black), and SP10C/CNF (red).

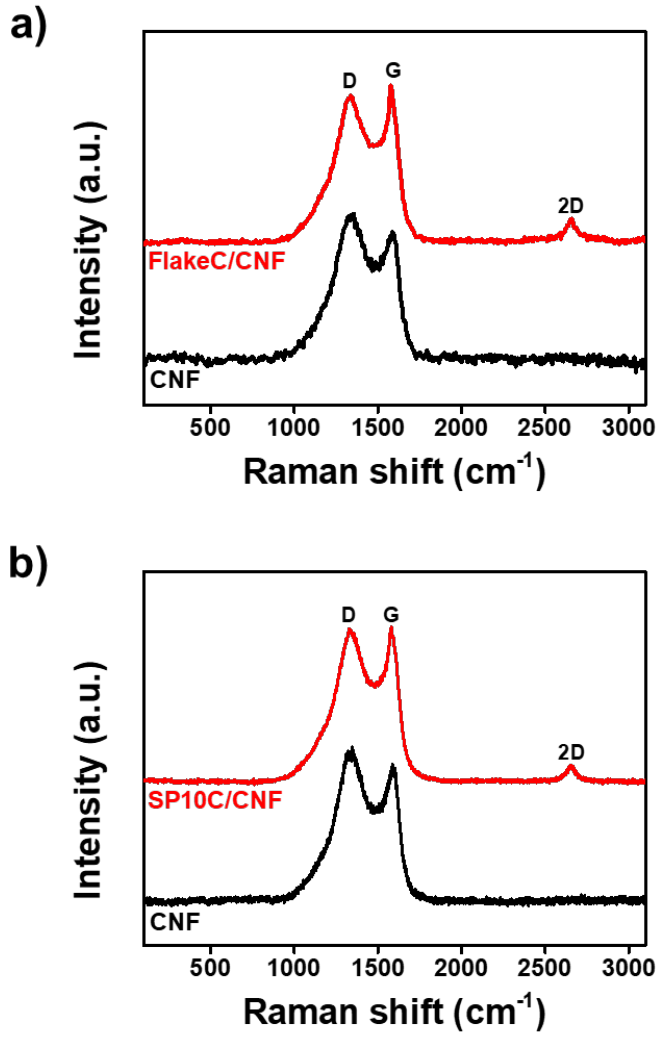

Figure 30. Raman spectra of (a) CNF (black), FlakeC/CNF (red), and (b) CNF (black), SP10C/CNF (red)

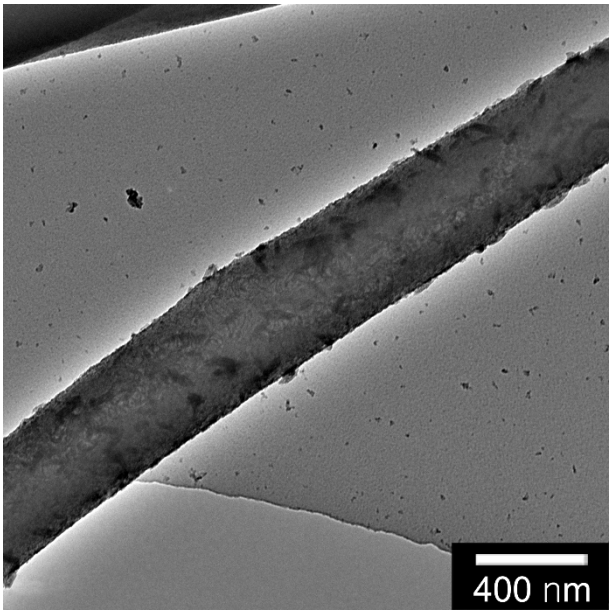

Figure 31. TEM image of SP10C/CNF

3.2.1. Fabrication of liquid-ion gated FET-type sensor electrode.

To investigate the electrical and sensing performance of the CuC/CNF mat, liquid-ion gated FET-type sensor configuration was constructed. **Figure 32** illustrates the sequential steps of sensor assemble procedures. First, a silver paste was printed *via* screen printing on the both end of the mat. Thereafter, binding aptamer and DMT-MM mixture was drop-cast on the CuC/CNF mat and dried in room temperature. The DMT-MM is well known organic triazine derivative that frequently used for amide synthesis. With the aid of DMT-MM, the PDGF-B binding aptamer which is modified with a primary aliphatic amino group at 5` end reacted with carboxyl group of carbon to form amide bond [146]. As a result, aptamer was successfully immobilized on CuC/CNF mat and aptamer functionalized CuC/CNF mat electrode had high stability with regard to surrounding environment owing to covalent bond between aptamer and CuC/CNF [147-149]. Aptamer functionalized FlakeC/CNF and SP10C/CNF are denoted as Apt-FlakeC/CNF, and Apt-SP10C/CNF respectively. The liquid-ion gated FET-type configuration was complete by adding 0.1 M PBS solution and applying voltage on prepared aptamer functionalized Cu/CNF mat electrode. In the FET-type sensor plot in

Figure 32, S, D, and V_G represent the source, drain, and gate electrodes, respectively.

In addition, **Figure 33** depicts FE-SEM image of aptamer functionalized SP10C/CNF mat. In high-resolution FE-SEM image, blunt surface and increased fiber thickness (*ca.* 420 nm) testified successfully aptamer immobilization [150].

Besides, actual photograph and resistance change caused by repeated bending were measured to prove the flexibility and free-standing properties of electrodes fabricated based on SP10C/CNF mat. The actual photograph confirmed that the SP10C/CNF mat based electrode was folded without damage (**Figure 34**). Additionally, excellent mechanical durability and flexibility were confirmed with 300 times of bending (**Figure 35**).

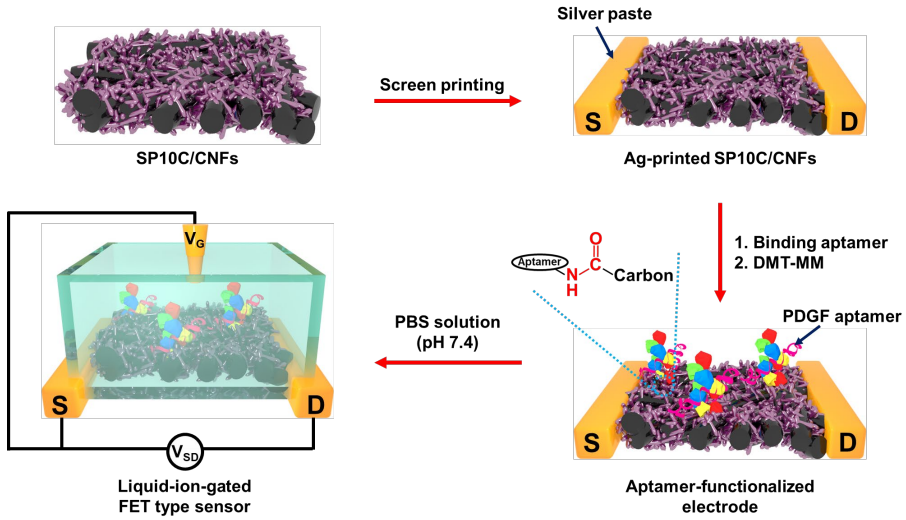

Figure 32. (a) Schematic illustration of fabrication steps for liquid-ion gated FET-type aptamer sensor.

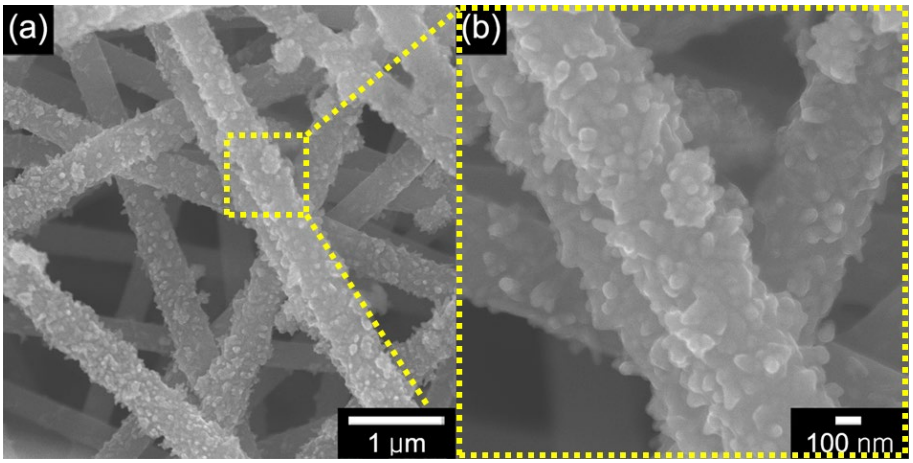

Figure 33. (a) Low- and (b) high resolution FE-SEM images of PDGF-B binding aptamer immobilized SP10C/CNF mat.

Figure 34. (a) Photograph of bent SP10C/CNF with screen printed silver paste electrode .

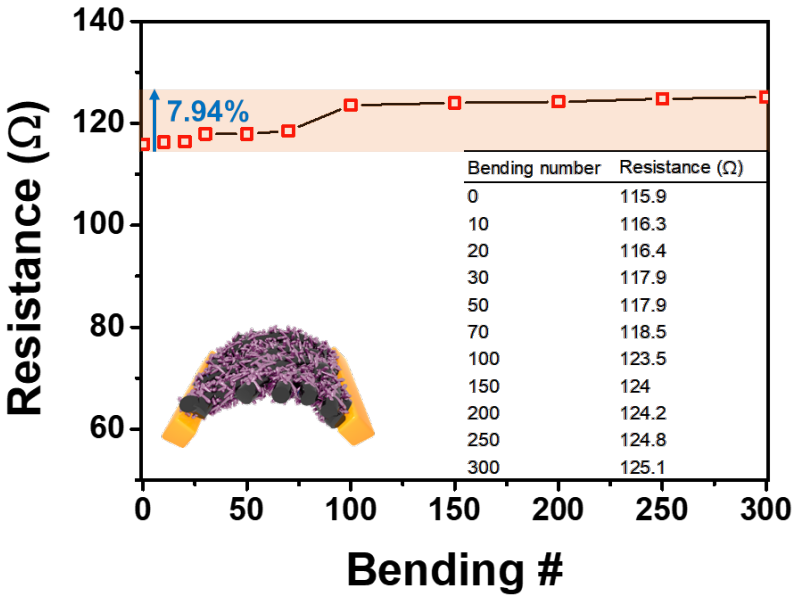

Figure 35. Resistance change of SP10C/CNF with repetitive bending.

3.2.1. Electrical properties of the CuC/CNF mat based sensor.

To confirm the electrical properties of the FlakeC/CNF, and SP10C/CNF mat were measured applying liquid ion gate voltage and source-drain voltage. Electrical contact and resistance were suggested by current-voltage (*I-V*) curves. As indicated in **Figure 36a**, *I-V* characteristic displays the ohmic contact (*i.e.,* linear) in wide voltage range, which is consider as good electrical contact as opposed to schottky barrier (*i.e.,* nonlinear). Moreover, Apt-SP10C/CNF mat exhibits linear behavior despite of aptamer immobilization. This result indicates that PDGF-B binding aptamer was successfully immobilized on SP10C/CNF mat by covalent bonding. The *dI/dV* value referred to as reciprocal of resistance. The FlakeC/CNF, and SP10C/CNF exhibit nearly similar slope value yet, increased *dI/dV* value was observed in aptamer immobilized case. However, since the order of *dV/dI* value did not changed, the electrical and sensing performance were maintained. To investigate charge transport properties liquid-ion gated FET-type configuration was adopted with applying PBS solution. **Figure 36b** shows the I_{SD}-V_{SD} curves with applying wide range V_G (-100 to -10 mV) at a constant scan rate of 10 mV s^{-1}. In constant V_{sd}, I_{sd} tended to increase negatively as V_G increased negatively. Namely, negative V_G increased the

oxidation level of the carbon channel, which means that it exhibits p-type behavior.

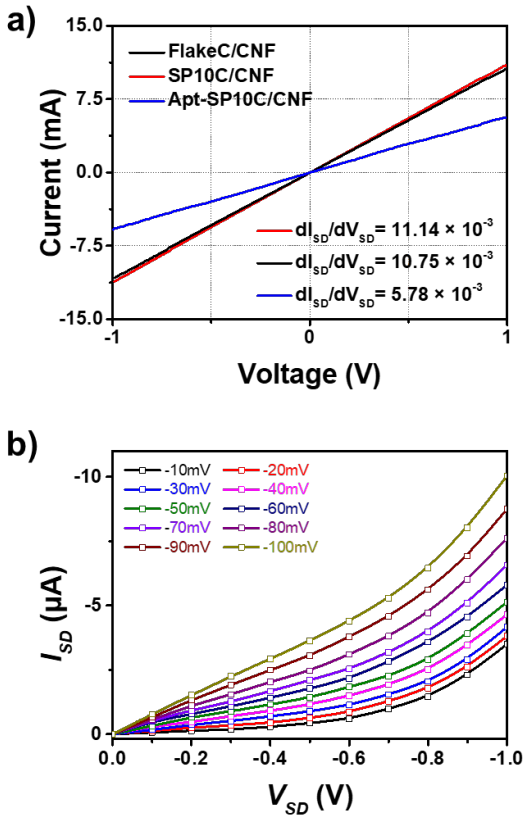

Figure 36. (a) Source-drain current versus source-drain voltage (I_{SD}-V_{SD}) for FlakeC/CNF (black), SP10C/CNF (red) and Apt-SP10C/CNF (blue), respectively. (b) I_{SD}-V_{SD} characteristics of Apt-SP10C/CNF based liquid-ion-gated FET sensors as a function of gate voltage (V_G) from -0.1 to -0.01 V (scan rate of V_{SD}: 10 mV s^{-1}).

3.2.1. Real-time response of the Apt-FlakeC/CNF and Apt-SP10C/CNF mat based sensor.

Figure 37a and b represents real-time response of the Apt-FlakeC/CNF and Apt-SP10C/CNF mat based PDGF sensors as a function of three different analyte concentration. The I_{SD} is monitored and normalized at a low operating voltage, (V_G = 10 mV, V_{SD}= 0.1 mV) with a sequential analyte injection. When injecting the target analyte (PDGF-AB and PDGF-BB), I_{sd} rapidly decreased and saturated within seconds. The decrease in I_{sd} accordance with the formation of a complex is owing to the interaction between the binding aptamer and the target analyte. In detail, aptamer generally show overall negative charge in PBS solution due to phosphate group in nucleic acid backbone. When target analyte was reacted with aptamer, morphology of aptamer change is induced from a linear form to complicated tertiary structure. The negative charge of the aptamer strand is weakened by chain folding, thereby decreasing the hole concentration on the surface of the sensor electrode and leading to decline in normalized current. This reaction occurs only in PDGF-AB and PDGF-BB, with PDGF-BB displaying a larger current change. This is because the aptamer stand is designed to react only with specific substances, similar to the substrate specificity of

the enzyme. As a result, PDGF-BB had lower minimum detectable level (MDL) than PDGF-AB at same sensor electrode. In addition to the type of target analyte, MDL also depends on the type of material that consist of the sensor electrode.

The apt-SP10C/CNF mat based sensor has an ultralow MDL of 1.78 fM, while the apt-FlakeC/CNF mat based sensor has a relatively high 1.78 pM MDL. This is because the protrusion on the surface of SP10C/CNF providing increased anchoring site for aptamer corresponding to high surface area. Additionally, injection of PDGF-AA in the FET-type sensor device couldn`t lead to current change due to absence of affinity with PDGF-B binding aptamer.

Figure 37c represents the sensitivity (S) calibration curve as a function of PDGF concentration. The sensitivity is defined as normalized current change from before target analyte inject to saturated value. Distinctively, PDGF sensors display the linear behavior with respect to wide range of PDGF-AB and PDGF-BB concentration. Formula of obtained curves are as follow:

$$S_{PDGF\text{-}AB}\ (\%) = -0.323\log C + 0.4539$$

$$S_{PDGF\text{-}BB}\ (\%) = -0.414\log C - 1.3368$$

$$S_{PDGF\text{-}AB}\ (\%) = -0.414\log C + 17708$$

$$S_{PDGF\text{-}BB}\ (\%) = -0.407 \log C + 0.3965$$

C: PDGF-AB or PDGF-BB concentration in fM.

When evaluating sensing performance of general sensor, selectivity is one of the most crucial part. Non-target molecules were selected with common serum protein (calmodulin (cal.), adenosine triphosphate(ATP), and bovine serum albumin (BSA)) to establish the specificity of the PDGF sensors. As shown in **Figure 38**, no significant current change was observed when injecting various non-target analyte (200 pM). On the contrary, exposure of 178 fM target molecules induced rapid decrease in normalized current which confirm the selectivity of PDGF sensors. Moreover, considering the incorporation of PDGF molecules with various substances in the body, real-time response was observed toward non-target mixtures. No significant current change was observed when the non-target mixture was added, but the non-target mixture with PDGF-BB 178 fM exhibited a rapid decrease in current. In addition, it was confirmed that the PBS solution only contributed to the dielectric layer formation by the absence of a significant current change even when injecting 0.1 M PBS solution.

Figure 39 presents the stability of SP10C/CNF mat based PDGF sensor with 178 fM PDGF-BB molecules. During stability test, sensor electrode was stored in a plastic vessel without any sealing and at room temperature. Under this condition, the sensitivity decreased by 12.14% for two weeks. This decrease is attributed to the inactivation of PDGF-BB aptamer and destruction of SP10C/CNF structure.

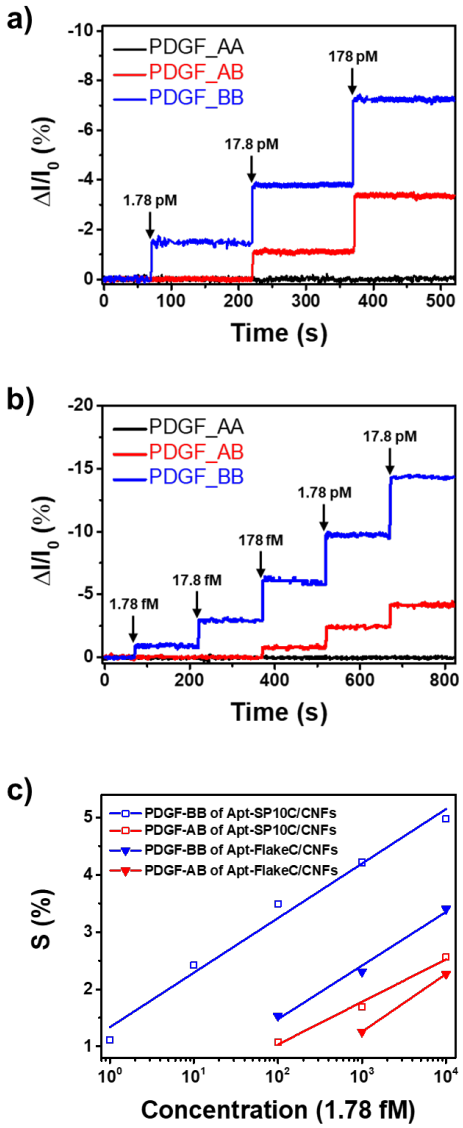

Figure 37. Real-time response with normalized current change of the (a) Apt-FlakeC/CNF mat and (b) Apt-SP10C/CNF mat toward PDGF-AA (black), PDGF-AB(red), and PDGF-BB (blue) (V_G: 10 mV, V_{SD}: 0.1 mV). (c) Calibration curve with target analyte concentration.

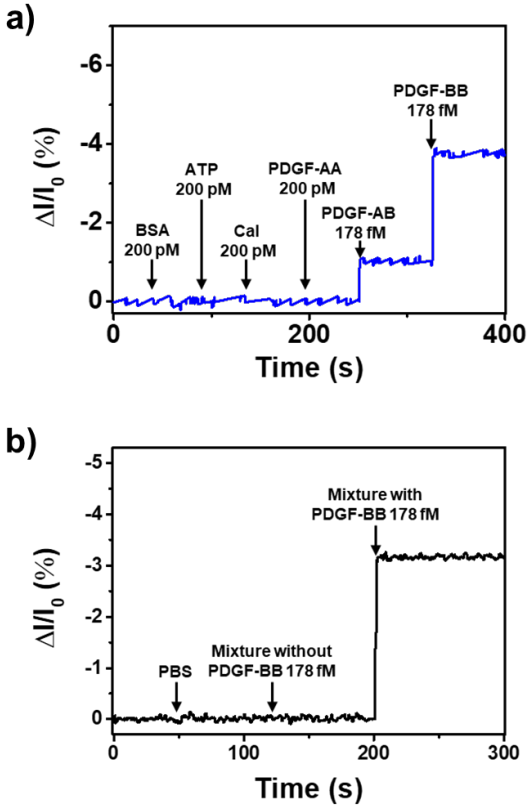

Figure 38. Selective response of Apt-SP10C/CNF mat toward target (PDGF-AB and PDGF-BB) and non-target (BSA, ATP, Cal., and PDGF-AA). (b) Selective response toward non-target mixture without PDGF-BB and with PDGF-BB.

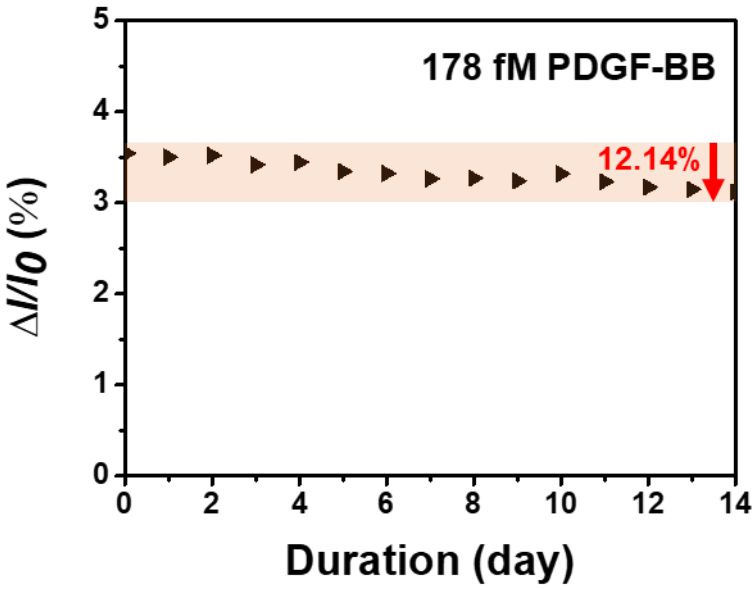

Figure 39. long-term stability of SP10C/CNF mat based PDGF sensor with exposure to 178 fM PDGF-BB.

3.3 Mn@CNF flexible and free-standing mat for DMMP gas sensor.

3.3.1. Fabrication of Mn@CNF mat

Figure 40 shows the schematic illustration of manganese dioxide decorated carbon nanofibers (Mn@CNF) fabrication process. First, PAN 13 wt% DMF solution prepared by vigorously stirring at 60 ℃ was used for electrospinning. The PAN NFs with a thickness of *ca*. 700 nm (**Figure 41a)** were prepared by electrospinning at 10 kV applied voltage between collector and metal needle with a flow rate of 5 μL min^{-1}. The electrospun PAN NFs were then, socked with deionized water to prevent tangling due to static electricity. The drenched PAN NFs were pressed at about 5 kg to reduce empty space between PAN NFs. Thereafter, the pressed PAN NFs were socked with ammonium persulfate (APS) 10% aqueous solution which is used as initiator for PPy polymerization. To coat PPy on PAN NFs surface, APS socked PAN NFs were exposed to vapor phase pyrrole monomer. The chemical reduction method was used to introduce manganese to the polypyrrole coated PAN NFs (PPy/PAN NFs) with a thickness of *ca.* 760 nm (**Figure 41b**). The PPy/PAN NFs were immersed into potassium permanganate ($KMnO_4$) 0.01M aqueous solution with 60 ℃, 30 min. Then, sheet-like amorphous MnO_2 was created on the surface of PPy/PAN NFs (a-MnO_2/PPy/PAN NFs) with a

thickness of *ca.* 1000 nm (**Figure 41c)**. The 2 step of heat treatment was then proceeded: first, stabilization process at 270 ℃ with 1 ℃ min^{-1} ramping rate and 1 h duration. Second, carbonization process at 700 ℃ with 5 ℃ min^{-1} ramping rate and 1 h duration. As a result, fabricated Mn@CNF with a thickness of *ca.* 500 nm were presented in **Figure 41d**. The stabilization assisted to convert the branched backbone structures of PPy and polyacrylonitrile into ring structure which enhanced the crystallinity of carbon materials. In general, carbon prepared using PAN 10% DMF solution is very brittle at macro-scale. In addition, $KMnO_4$ treatment also increased the brittle nature because it is proceeded with harsh condition. To overcome this disadvantage, thicker PAN NFs were prepared using PAN 13% solution, followed by compression and PPy coating. As a consequence, flexible and free-standing Mn@CNF mat was achieved (**Figure 42**).

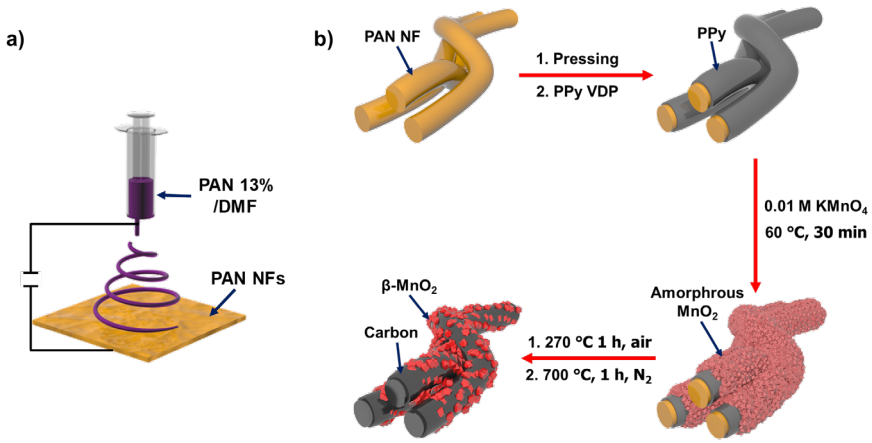

Figure 40. (a) Schematic illustration of electrospinning process, and (b) The sequential fabrication step of manganese dioxide@carbon nanofibers (Mn@CNF).

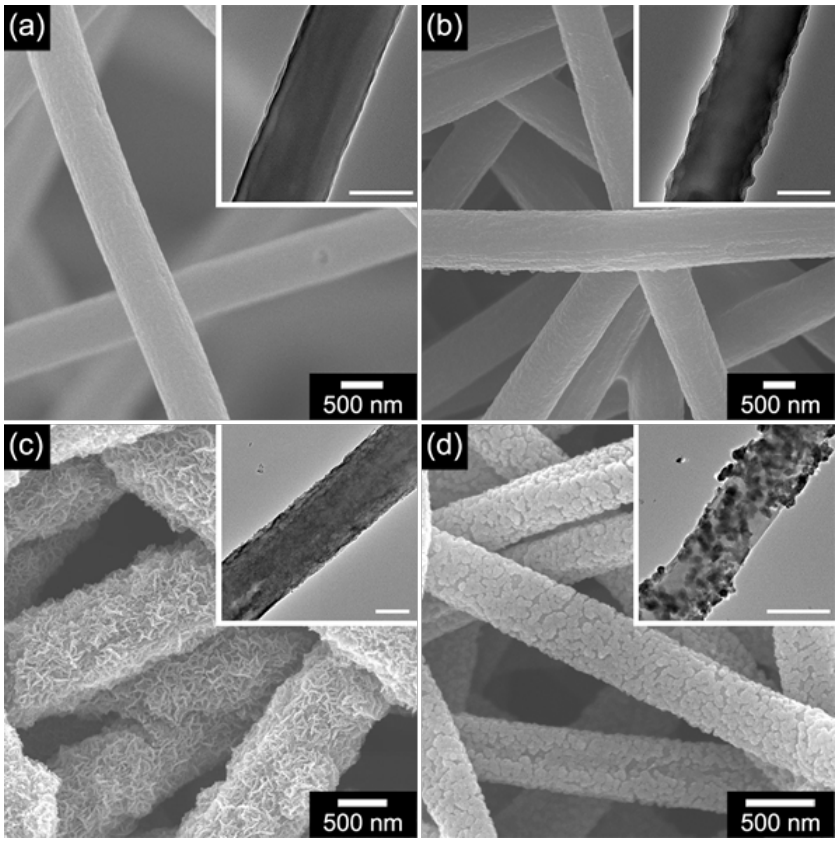

Figure 41. SEM and TEM (inset) images of (a) PAN NFs, (b) PPy/PAN NFs, (c) a-MnO_2/PPy/PAN, and (d) Mn@CNF. (scale bar of inset :500nm)

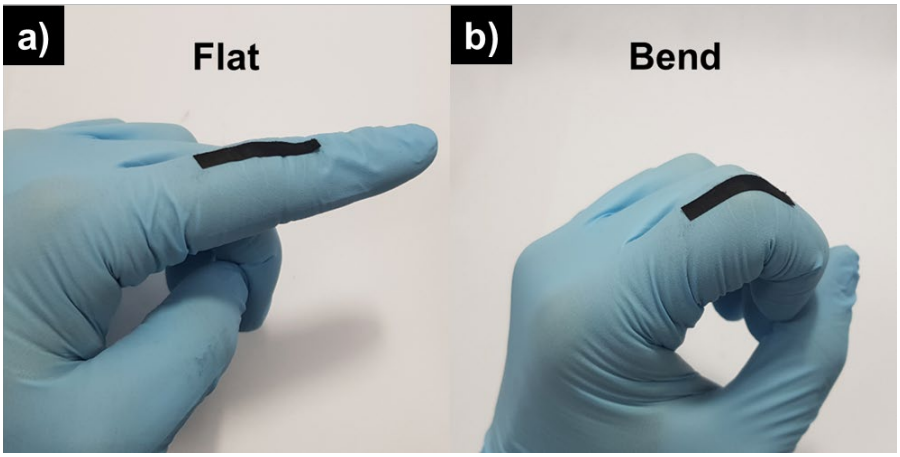

Figure 42. Flat and bent Mn@CNF mat attached on nitrile glove.

3.3.2. Characterization of Mn@CNF mat

The chemical composition was investigated using X-ray photoelectron spectroscopy (XPS). **Figure 43a** displays the wide scan XPS spectra over range of 0 to 800 eV. The Mn@CNF spectrum demonstrates the presence of Mn by Mn 2p, Mn 3s, and Mn 3p peaks. On the other hand, CNF produced by stabilization and carbonization of PAN NFs without any treatment did not display Mn related peaks. Furthermore, the high resolution XPS spectra of Mn 2p revealed that $2p_{1/2}$ and $2p_{3/2}$ spin-orbit components (observed at 644.5 and 653.3 eV, respectively) are major state of Mn. This confirm that the major state of Mn introduced on CNF is Mn^{4+} which demonstrate the presence of the MnO_2 (**Figure 43b**). As for the O 1s spectra, biggest peak (binding energy at 529.84 eV) may attribute to Mn-O bond, while binding energy at 531.20 and 532.18 peaks arose from OH^- radical, adsorbed oxygen, or carbonyl group, and adsorbed water on the outside respectively (**Figure 43c**). In C 1s spectra, strongest peak at 284.60 eV is referred to C-C bond that existed in carbon structure, while binding energy at 285.83 and 288.05 eV are resulting from oxygen containing functional groups (**Figure 43d**) [151-152]. Furthermore, X-ray diffraction spectra was adopted to demonstrate the presence and crystallinity of MnO_2 (**Figure 44a**). In a-MnO_2/PPy/PAN

NFs, peaks associated with crystallinity did not appear, whereas in Mn@CNF spectrum, characteristic diffraction peaks at the 2θ angle of 34.98°, 40.60°, and 58.72°, corresponding to the (110), (101), and (211) respectively, identified the β-MnO_2 [153-154]. **Figure 44b** exhibits the Raman spectra ranging from 200 to 2500 cm^{-1}. The typical β-MnO_2 peaks at 650 cm^{-1} indicate the stretching mode of MnO_6 octahedral and two small weak peaks at 362, and 302 cm^{-1} originated from the bending mode of O-Mn-O or minor portion of Mn_2O_3, Mn_3O_4. Additionally, EDX element dot mapping analysis confirmed that Mn, and N were uniformly existed through the nanomaterials (**Figure 45**) [155-156].

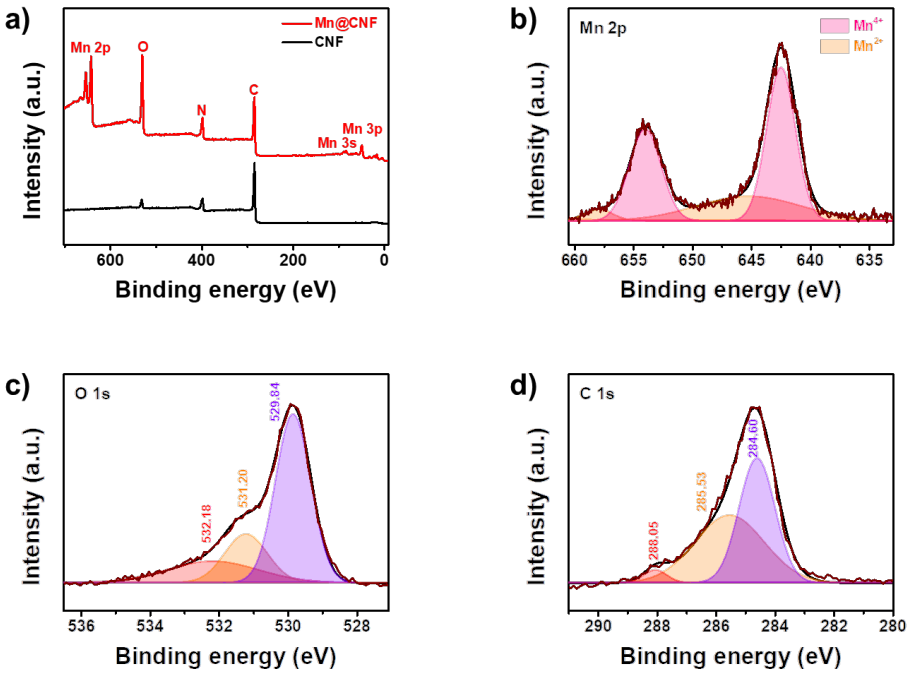

Figure 43. (a) full scanned XPS spectra of CNF (black), and Mn@CNF (red). (b) Mn 2p, (c) O 1s, and (d) C 1s XPS spectra of Mn@CNF.

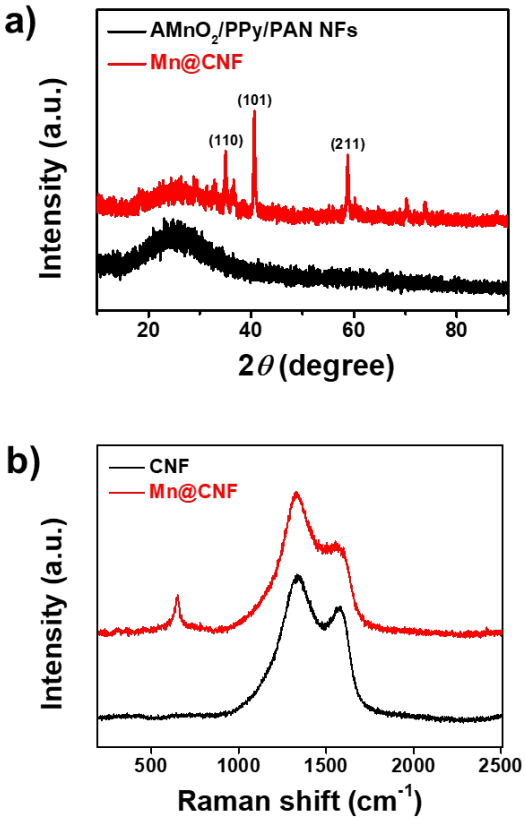

Figure 44. (a) XRD data acquired from a-MnO_2/PPy/PAN NFs (black), and Mn@CNF (red). (b) Raman spectra of CNF (black), and Mn@CNF (red).

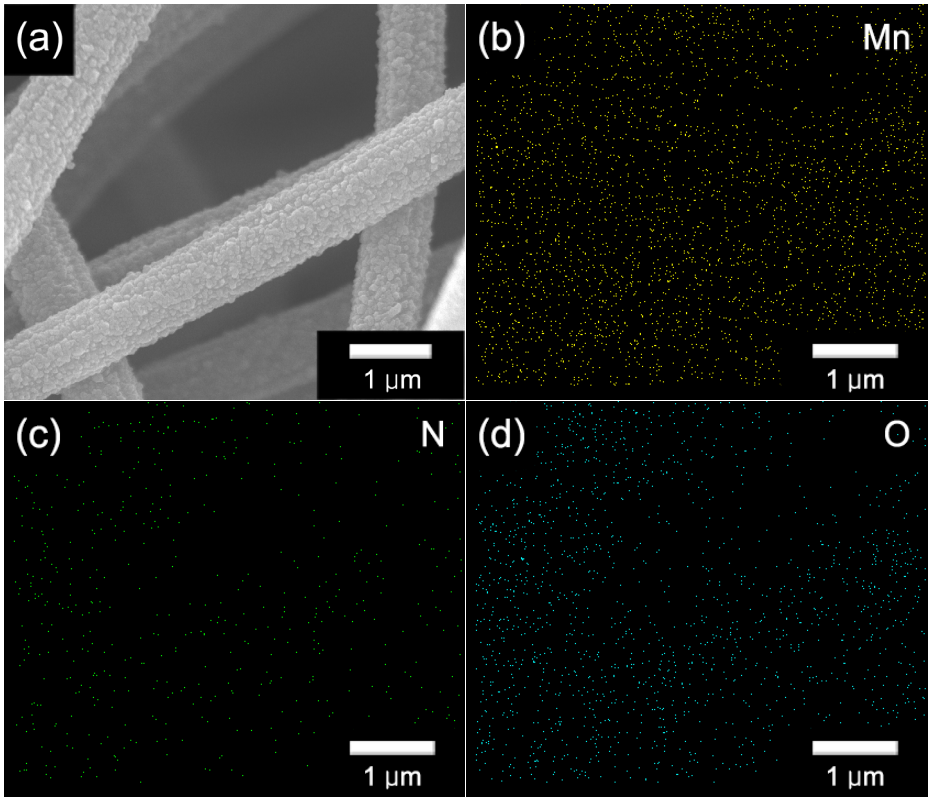

Figure 45. (a) SEM and EDX mapping of element (b) Mn, (c) N, and (d) O images of Mn@CNF.

3.3.3. Electrical properties and real-time responses of Mn@CNF based sensor to DMMP gas

The Mn@CNF flexible mat immediately detects DMMP gas based on charge transfer mechanism. When Mn@CNF mat was exposed to DMMP gas, both CNF and MnO_2 are involved in gas detection process *via* creating the continuous charge transfer pathway. DMMP gas is a strong electron donor that provides electrons when adsorbed onto CNF. This increases the electrical resistance by lowering the hole concentration in the CNF. The change in hole concentration in CNF is further enhanced by chemical absorption of MnO_2 and DMMP gas. The DMMP gas is adsorbed by charge interaction which is match up with interaction between lone pair electron of methoxy O atom and the vacant orbital of an acidic surface site of Mn^{4+} atom. As a result, electrons flow from the DMMP gas to CNF, which causes an increase in electrical resistance. The synergy of these two effects makes it possible to operate at room temperature, whereas sensors made only of metal oxides have high operating temperatures. (**Figure 46**)

Figure 47a displays the current-voltage (*I-V*) of the Mn@CNF mat. The linear behavior of *I-V* curve corresponding to the high uniformity of Mn@CNF mat. Additionally, initial resistance of mat could be calculated

by reciprocal of slope (*ca.* 133.3 kΩ). **Figure 47b** represents the response of bare CNF and Mn@CNF electrode with sequential exposure to DMMP gas. Mn@CNF sensor displayed larger response and lower limit of detection concentration than CNF sensor due to as described DMMP sensing mechanism. **Figure 47c** present the normalized resistance response upon periodic exposure to DMMP gas as a function of various analyte concentration. The sensor certified the similar resistance change behavior in both response and recovery over 4 cycles. Additionally, Mn@CNF sensors showed linear change in sensitivity as a function of log-scale analyte concentration (**Figure 47d**).

The limit of detection was obtained using the statement that resistance changes with a signal to noise (S/N) ratio of less than 3 cannot be consider as non-significant change. In the range where the normalized resistance change ($\Delta R/R_0$%) displays the linear behavior with analyte concentration, DMMP sensing was conducted and linear fit was performed (**Figure 48a and b**). Then, 5th polynomial fit was executed in the range of before exposure to DMMP gas. (**Figure 48c**)

$$\mathrm{RMS_{Noise}} = \sqrt{\frac{V_X^2}{N-1}}, \text{in which } V_X^2 = \sum (Y_i - Y)^2$$

$$\mathrm{LOD} = \frac{\mathrm{RMS_{Noise}}}{\mathrm{Slope}}$$

Y_i: chosen data point at the baseline of response verse time curve before exposure of the DMMP gas (In this study, I take 11 data point. N=11)

Y: corresponding value calculated form the fitted curve

The limit of detection obtained using the equation above is 0.108 ppb, which corresponds to the lowest response concentration in **Figure 47** (**Table 1**) [157].

Stability and selectivity is one of the most critical part of the sensors. **Figure 49a** presents the result of long-term stability test based on Mn@CNF mat for DMMP sensors. During the 30-day experiment, only 12.76% decrease in normalized resistance change was demonstrated. This is because carbon, which is not easily transformed or decomposed by the surrounding environment such as humid, light, and temperature, forms the basis of the Mn@CNF mat. **Figure 49b** indicates the selectivity toward various volatile organic compounds (VOCs) at room temperature. These VOCs were selected as materials with functional groups capable of interacting similarly to sensor-DMMP. The vapors were introduced in the same way as DMMP gas, but showed lower resistance change. This is because the acceptor group (-OCH_3) in DMMP

has higher polarity (3.62 D) than the functional group in VOCs. Since the larger partial charges have stronger interaction with Mn^{4+}, the Mn@CNF mat sensor had great selectivity toward DMMP.

To verify flexibility, I measured the properties according to the degree of bending. The bending angle was defined as the angle between one end-center-other end of the mat. The *I-V* curve was measured to see the change in resistance with bending. As illustrated in **Figure 50a**, despite the distortion, linear behavior and electrical resistance was sustained. In addition, there was no significant influence on signal change when sensing with 0.1 ppb DMMP gas (**Figure 50b**). Furthermore, repetitive bending test was conducted to identify the electrical resistance change (**Figure 51**). Despite 300 times of repetitions, the electrical resistance increased by only 18.09%. Considering the above result, Mn@CNF mat can be applied as DMMP sensor in a flexible and free-standing manner.

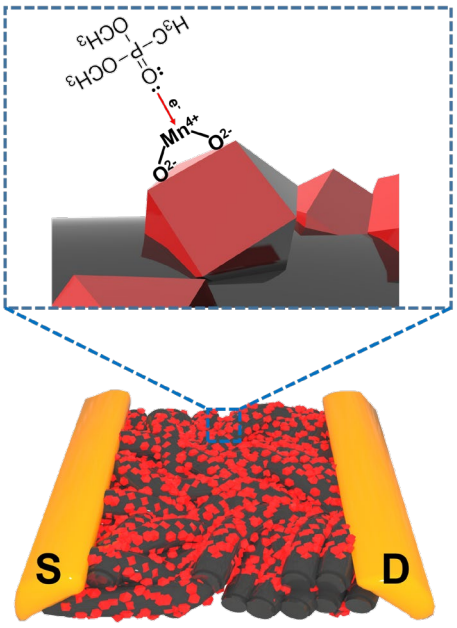

Figure 46. schematic illustration of DMMP gas sensing mechanism.

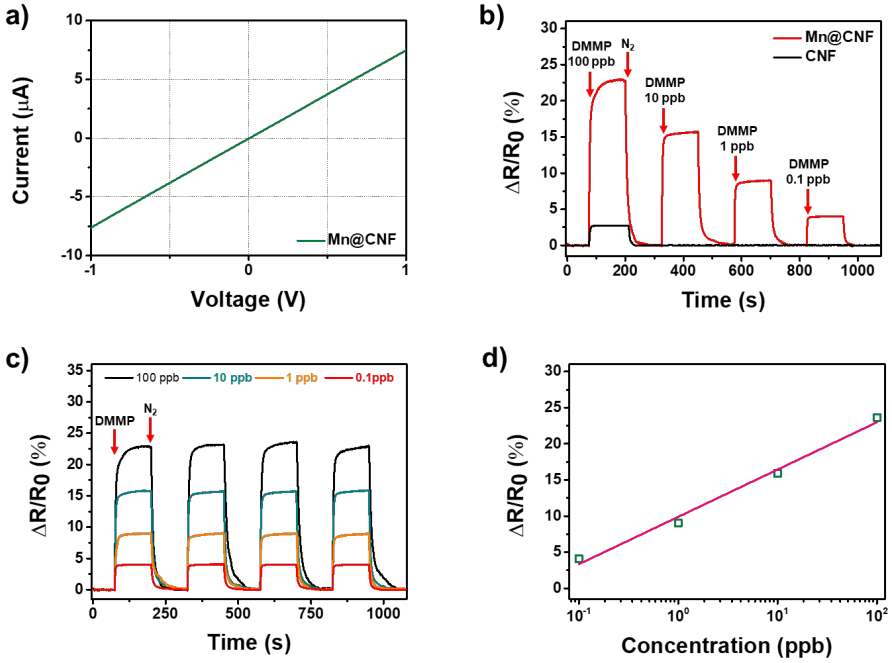

Figure 47. (a) Current-voltage (*I-V*) relationships of Mn@CNF sensor. (b) Reversible and reproducible real-time responses of CNF (black), and Mn@CNF (red) in concentration range from 0.1 to 100 ppb. (c) Sequential exposure to various DMMP vapor concentration. (d) calibration curve of Mn@CNF with log scale.

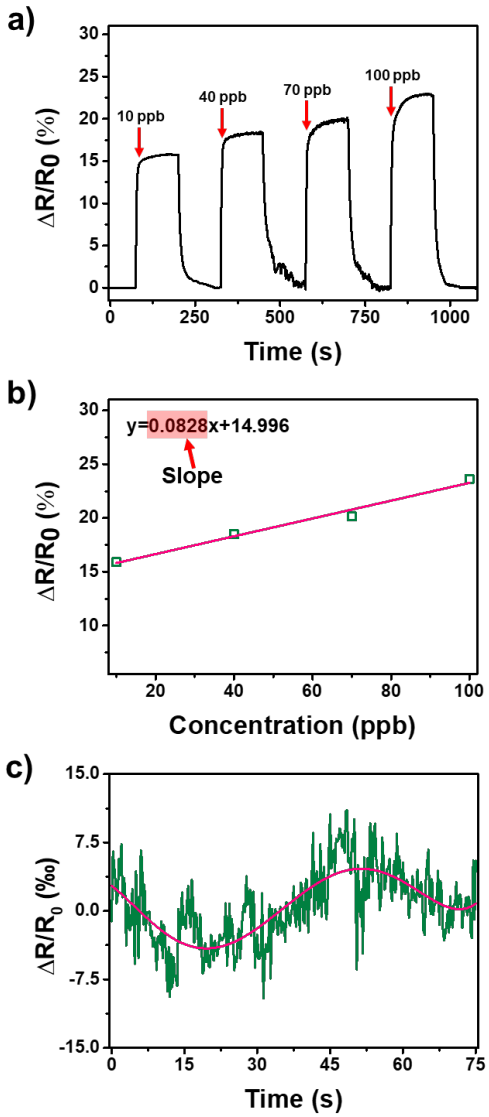

Figure 48. (a) Real-time responses of Mn@CNF in concentration range from 10 to 100 ppb. (b) calibration line of Mn@CNF as a function of DMMP concentration. (c) Plot of 5th order polynomial fitted normalized resistance change before exposure to DMMP gas.

Table 1. Calculation of LOD in Mn@CNF based DMMP detection.

Slope (ppb^{-1})	V_x^2	RMS_{noise}(%)	LOD (ppb)
0.08280	0.00266	0.00298	0.10795

Y_i ,data at the baseline Y, Corrresponding value calculated from fitted curve
$RMS_{Noise}=\sqrt{(V_x^2/(N-1))}$, in which $V_x^2 = \sum(Y_i-Y)^2$, N=number of data point
$LOD=3\times RMS_{Noise}/Slope$

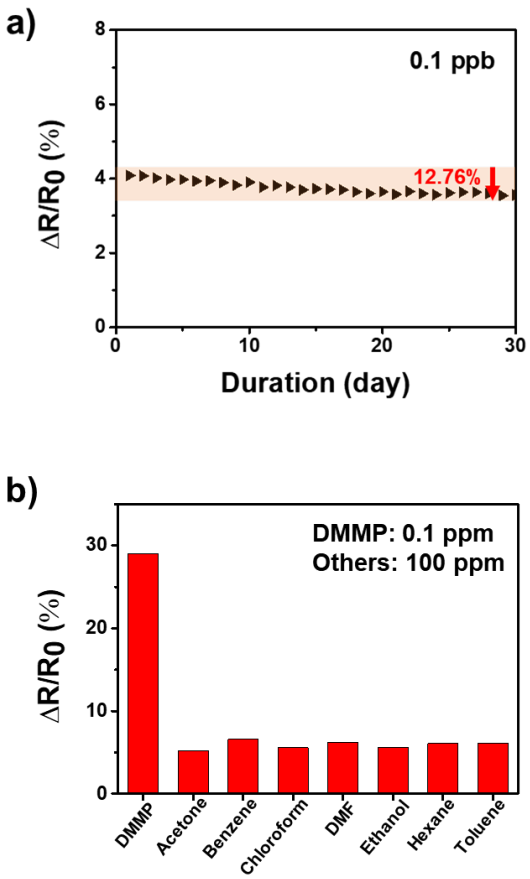

Figure 49. (a) Long-term stability of Mn@CNF structure with exposure to 0.1 (b) Selective characteristic of Mn@CNF sensor with respect to 0.1 ppb DMMP and various non-target gas (100 ppm of acetone, benzene, chloroform, DMF, ethanol, hexane, and toluene).

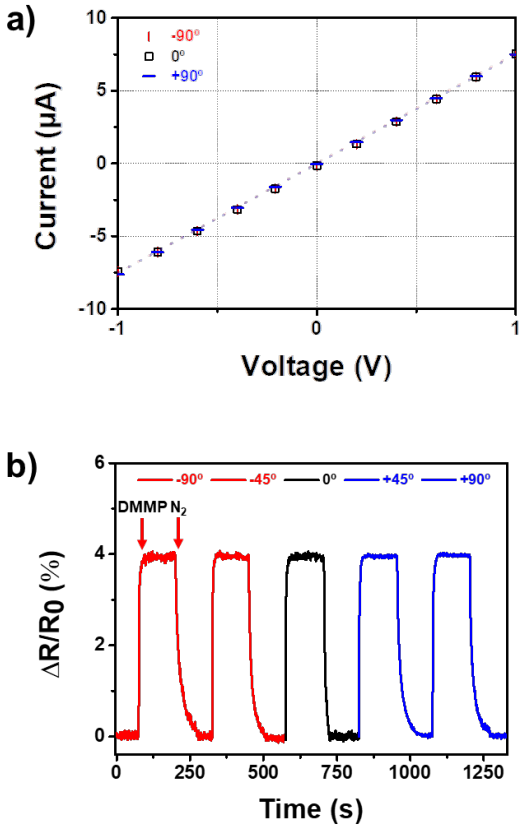

Figure 50. (a) current-voltage curve with various bending angles of Mn@CNF electrode. (b) normalized resistance change with various bending angles of Mn@CNF electrode.

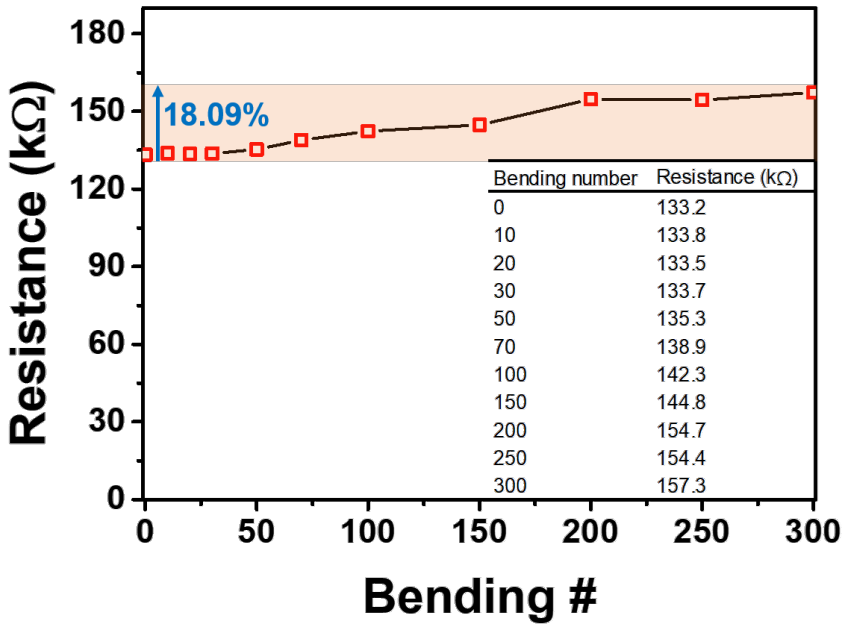

Figure 51. Resistance change of Mn@CNF with repetitive bending.

4. Conclusion

The various sorts of electrospun polyacrylonitrile nanofibers based materials were fabricated *via* vapor phase deposition, electrodeposition, chemical reduction of metal ion, chemical vapor deposition (VDP), and carbonization method. These fabricated materials were used as biosensor and chemiresistive gas sensor. Additionally, these prepared materials suggested potential in diverse sensing area with flexibility and free-standing property. The subtopics could be concluded as following:

1. I fabricate polypyrrole/polyacrylonitrile nanofibers (PPy/PAN NFs) and palladium (Pd) decorated PPy/PAN NFs using electrospinning with polymer solution, VDP of polypyrrole, and electrodeposition. During electrodeposition, shape of Pd was controlled by sulfuric acid concentration in electrolyte. In addition, Pds were uniformly decorated on the surface of PPy/PAN NFs without any aggregation due to carboxyl group came from 3-carboxylated pyrrole monomer. This Pd_PPy/PAN NFs were characterized by FE-SEM, TEM, XPS, XRD and Raman. The unique flower-like Pd structure facilitated the ultralow MDL (1 nM) in Pd_PPy/PAN NFs based non-enzyme sensor for H_2O_2.

2. I fabricated the copper derived carbon/carbon nanofiber (CuC/CNF) mat with using flake and sphere type Cu. To prepare unique structure, polymer chain stabilization through heat treatment at room temperature and CVD process with Cu etching were conducted. The morphology of Cu derived carbon was determined by original shape of Cu and Cu etching process. In the case of using sphere type Cu, protrusions formation and Cu derived carbon wrapping CNF are simultaneously generated due to metal etching, resulting in a unique shape. The aptamer FET type biosensor configuration was conducted by amine modified PDGF-B binding aptamer immobilization on the surface of CuC/CNF mat *via* amide covalent bonding and liquid electrolyte gate using PBS solution. As fabricated PDGF-B sensor showed real-time response toward PDGF-AB and PDGF-BB with very low MDL (1.78 fM) and high selectivity. The long term stability owing to covalent bonding between aptamer and CuC/CNF mat was testified. Furthermore, it is highly applicable to various types of sensors in biological and environmental research in that the electrode material is flexible and free-standing.

3. I fabricated manganese dioxide decorated carbon nanofiber

(Mn@CNF) mat and demonstrated its use as a high performance transducer for chemiresistive sensor. To produce crystalline β-MnO_2, chemical reduction was used for reduction of metal oxide precursor and heat treatment was adopted for changing amorphous to crystalline. The Mn@CNF mat could detect DMMP with high sensitivity (MDL of 0.1 ppb) and long-term stability at room temperature. Furthermore, flexible and free-standing properties of Mn@CNF mat prevent performance degradation when the Mn@CNF mat was bent with various angle. Namely, this novel approach incorporating the low operating temperature and bendability, is expected to apply in various gas sensors.

References

[1] H. Shirakawa, *Angew. Chem*. *Int. Ed.* **2001**, *40*, 2574-2580.

[2] A. G. MacDiarmid, *Angew. Chem. Int. Ed.* **2001**, *40* 2581-2590.

[3] A. J. Heeger, *Angew. Chem. Int. Ed.* **2001**, *40*, 2591-2611.

[4] C. Zhan, G. Yu, Y. Lu, L. Wang, E. Wujcik, S. Wei, *J. Mater. Chem. C* **2017**, *5*, 1569-1585.

[5] T. H. Le, Y. Kim, H. Yoon, *Polymers* **2017**, *9*.

[6] A. O. PAUL, A. J. HEEGER, F. WUDL, *Chem. Rev.* **1988**, *88*, 183-200.

[7] C. Wu, J. Z. Ou, F. He, J. Ding, W. Luo, M. Wu, H. Zhang, *Nano Energy* **2019**, *65*.

[8] E. M. GENIES, G. BIDAN, *J. Electroanal. Chem.* **1983**, *149*, 101-113.

[9] B. Chethan, H. G. R. Prakash, Y. T. Ravikiran, S. C. Vijayakumari, S. Thomas, *Sens. Actuators B-Chem.* **2019**, *296*, 126639

[10] L. Wang, S. Li, F. Huang, X. Yu, M. Liu, H. Zhang, *J. Power Sources* **2019**, *439*.

[11] J. Jang, J. H. Oh, X. L. Li, *J. Mater. Chem.* **2004**, *14*.

[12] P. Camurlu, *RSC Adv.* **2014**, *4*, 55832-55845.

[13] J. E. Lee, S. J. Park, O. S. Kwon, H. W. Shim, J. Jang, H. Yoon, *RSC Adv.* **2014**, *4*.

[14] J. Jang, B. Lim, M. Choi, *Chem. Commun.* **2005**, 4214-4216.

[15] K. Kim, J.-I. Jin, *Nano Lett.* **2001**, *1*, 631-636.

[16] J. S. Lee, D. H. Shin, J. Jang, *Energy Environ. Sci.* **2015**, *8*, 3030-3039.

[17] S. J. Park, O. S. Kwon, J. Jang, *Chem. Commun.* **2013**, *49*, 4673-4675.

[18] J. S. Lee, D. H. Shin, W. Kim, J. Jang, *J. Mater. Chem. A* **2016**, *4*, 6603-6609.

[19] J. W. Park, W. Na, J. Jang, *J. Mater. Chem. A* **2016**, *4*, 8263-8271.

[20] J. Jang, B. Lim, *Angew. Chem. Int. Ed.* **2003**, *42*, 5600-5603.

[21] Z. Liu, A. W. A. Murphy, C. Kuppe, D. C. Hooper, V. K. Valev, A. Ilie, *ACS Nano* **2019**, *13*, 3896-3909.

[22] H. D. Tran, D. Li, R. B. Kaner, *Adv. Mater.* **2009**, *21*, 1487-1499.

[23] X. Lu, C. Wang, F. Favier, N. Pinna, *Adv. Energy Mater.* **2017**, *7*.

[24] M. R. Abidian, D. H. Kim, D. C. Martin, *Adv. Mater.* **2006**, *18*, 405-409.

[25] H.-G. Wang, S. Yuan, D.-L. Ma, X.-B. Zhang, J.-M. Yan, *Energy Environ. Sci.* **2015**, *8*, 1660-1681.

[26] U. Kumar, B. C. Yadav, *Sens. Actuators B-Chem.* **2019**, *288*, 399-407.

[27] V. V. Pokropivny, V. V. Skorokhod, *Physica E* **2007**, *40*, 2521-2525.

[28] Z. Yin, Q. Zheng, *Adv. Energy Mater.* **2012**, *2*, 179-218.

[29] G. H. Kim, H. Nam, W. Choi, T. An, G. Lim, *Adv. Mater.*

Interfaces **2018**, *5*.

[30] J. H. Lee, J. Kim, D. Liu, F. Guo, X. Shen, Q. Zheng, S. Jeon, J. K. Kim, *Adv. Funct. Mater.* **2019**, *29*.

[31] J. Xue, T. Wu, Y. Dai, Y. Xia, *Chem. Rev.* **2019**, *119*, 5298-5415.

[32] J. Yoon, H. S. Yang, B. S. Lee, W. R. Yu, *Adv. Mater.* **2018**, *30*, e1704765.

[33] D. Li, Y. Xia, *Adv. Mater.* **2004**, *16*, 1151-1170.

[34] S. R. Merritt, A. A. Exner, Z. Lee, H. A. von Recum, *Adv. Eng. Mater.* **2012**, *14*, B266-B278.

[35] Z. Dai, P.-G. Ren, Y.-L. Jin, H. Zhang, F. Ren, Q. Zhang, *J. Power Sources* **2019**, *437*.

[36] C.-L. Zhang, Z.-H. Jiang, B.-R. Lu, J.-T. Liu, F.-H. Cao, H. Li, Z.-L. Yu, S.-H. Yu, *Nano Energy* **2019**, *61*, 104-110.

[37] Y. Xue, X. Guo, H. Zhou, J. Zhou, *Carbon* **2019**, *154*, 219-229.

[38] H. Wang, X. Yang, Q. Wu, Q. Zhang, H. Chen, H. Jing, J. Wang, S. B. Mi, A. L. Rogach, C. Niu, *ACS Nano* **2018**, *12*, 3406-3416.

[39] H. Jia, N. Sun, M. Dirican, Y. Li, C. Chen, P. Zhu, C. Yan, J. Zang, J. Guo, J. Tao, J. Wang, F. Tang, X. Zhang, *ACS Appl. Mater. Interfaces* **2018**, *10*, 44368-44375.

[40] C. Liu, N. Xiao, Y. Wang, Y. Zhou, G. Wang, H. Li, Y. Ji, J. Qiu, *Carbon* **2018**, *139*, 716-724.

[41] A. S. Levitt, M. Alhabeb, C. B. Hatter, A. Sarycheva, G. Dion, Y. Gogotsi, *J. Mater. Chem. A* **2019**, *7*, 269-277.

[42] D. B. Cairns, M. A. Khan, C. Perruchot, A. Riede, S. P. Armes, *Chem. Mater.* **2003**, *15*, 233-239.

[43] S. F. Lascelles, S. P. Armes, *J. Mater. Chem.***1997**, *7*, 1339-1347.

[44] Inamuddin, H. Abbas Kashmery, *Sci. Rep.* **2019**, *9*, 9877.

[45] D. Zhang, Z. Yang, P. Li, X. Zhou, *Sens. Actuators B-Chem.* **2019**, *301*.

[46] Y. Sun, R. Han, Y. Dai, X. Zhu, H. Liu, D. Gao, C. Luo, X. Wang, Q. Wei, *Sens. Actuators B-Chem.* **2019**, *301*.

[47] S. Zeng, X. Li, M. Li, J. Zheng, S. E, W. Yang, B. Zhao, X. Guo, R. Zhang, *Carbon* **2019**, *155*, 34-43.

[48] Q. Wu, J. Wu, G. S. Wang, H. Z. Zhang, H. J. Gao, W. J. Shui, *Sci. Rep.* **2019**, *9*, 10488.

[49] Z. Liu, S. Poyraz, Y. Liu, X. Zhang, *Nanoscale* **2012**, *4*, 106-109.

[50] H. Zhang, Y. Liu, J. Wu, B. Xin, *J Colloid Interface Sci.* **2016**, *476*, 214-221.

[51] L. Yang, Z. Zhang, G. Nie, C. Wang, X. Lu, *J. Mater. Chem. A* **2015**, *3*, 83-86.

[52] B. Wu, N. Zhao, S. Hou, C. Zhang, *Nanomaterials* **2016**, *6*.

[53] J. Han, M. Wang, Y. Hu, C. Zhou, R. Guo, *Prog. Polym. Sci.* **2017**, *70*, 52-91.

[54] I. Sapurina, J. Stejskal, I. Šeděnková, M. Trchová, J. Kovářová, J. Hromádková, J. Kopecká, M. Cieslar, A. Abu El-Nasr, M. M. Ayad, *Synth. Met* **2016**, *214*, 14-22.

[55] W. Guo, J. Jiao, K. Tian, Y. Tang, Y. Jia, R. Li, Z. Xu, H. Wang, *RSC Adv.***2015**, *5*, 102210-102218.

[56] S. S. Sainudeen, L. B. Asok, A. Varghese, A. S. Nair, G. Krishnan, *RSC Adv.***2017**, *7*, 35160-35168.

[57] G. Zhang, H. B. Wu, H. E. Hoster, X. W. Lou, *Energy Environ. Sci.* **2014**, *7*, 302-305.

[58] M. Zhi, C. Xiang, J. Li, M. Li, N. Wu, *Nanoscale* **2013**, *5*, 72-88.

[59] D. Feng, T.-N. Gao, M. Fan, A. Li, K. Li, T. Wang, Q. Huo, Z.-A. Qiao, *NPG Asia Mater.* **2018**, *10*, 800-809.

[60] Y. Liu, J. Ma, T. Lu, L. Pan, *Sci. Rep.* **2016**, *6*, 32784.

[61] I. T. Kim, S. Shin, M. W. Shin, *Carbon* **2018**, *135*, 35-43.

[62] A. Jagadale, X. Zhou, D. Blaisdell, S. Yang, *Sci. Rep.* **2018**, *8*, 1602.

[63] S. M. S, E. Adabifiroozjaei, Y. Yao, P. Koshy, S. Lim, R. Webster, X. Liu, R. Khayyam Nekouei, C. Cazorla, Z. Liu, Y. Wang, N. Lambropoulos, C. C. Sorrell, *Nat. Commun.* **2019**, *10*, 2594.

[64] D.-K. Kim, H. Kim, H. Park, S. Oh, S. H. Ahn, H.-J. Kim, S.-K. Kim, *J. Power Sources* **2019**, *438*.

[65] T. Zhou, L. Yan, C. Xie, P. Li, L. Jiang, J. Fang, C. Zhao, F. Ren, K. Wang, Y. Wang, H. Zhang, T. Guo, X. Lu, *Small* **2019**, *15*, e1805440.

[66] J. Ding, Z. Liu, X. Liu, J. Liu, Y. Deng, X. Han, C. Zhong, W. Hu, *Adv. Energy Mater.* **2019**, *9*.

[67] G. Barati Darband, M. Aliofkhazraei, S. Hyun, A. Sabour Rouhaghdam, S. Shanmugam, *Nanoscale* **2019**, *11*, 16621-16634.

[68] F. Du, Y. Zhang, H. He, T. Li, G. Wen, Y. Zhou, Z. Zou, *J. Power Sources* **2019**, *431*, 182-188.

[69] C. Liu, T. Wu, P. C. Hsu, J. Xie, J. Zhao, K. Liu, J. Sun, J. Xu, J. Tang, Z. Ye, D. Lin, Y. Cui, *ACS Nano* **2019**, *13*, 6431-6437.

[70] Z. Yan, H. Sun, X. Chen, H. Liu, Y. Zhao, H. Li, W. Xie, F. Cheng, J. Chen, *Nat. Commun.* **2018**, *9*, 2373.

[71] P. Lobaccaro, A. Raygani, A. Oriani, N. Miani, A. Piotto, R. Kapadia, M. Zheng, Z. Yu, L. Magagnin, D. C. Chrzan, R. Maboudian, A. Javey, *J. Electrochem. Soc.***2014**, *161*, D794-D800.

[72] M. Jin, H.-K. Jeong, T.-H. Kim, K. P. So, Y. Cui, W. J. Yu, E. J. Ra, Y. H. Lee, *J. Phys. D Appl. Phys.***2010**, *43*.

[73] H. Yu, B. Zhang, C. Bulin, R. Li, R. Xing, *Sci. Rep.* **2016**, *6*, 36143.

[74] S. Bae, H. Kim, Y. Lee, X. Xu, J. S. Park, Y. Zheng, J. Balakrishnan, T. Lei, H. R. Kim, Y. I. Song, Y. J. Kim, K. S. Kim, B. Ozyilmaz, J. H. Ahn, B. H. Hong, S. Iijima, *Nat. Nanotechnol.* **2010**, *5*, 574-578.

[75] J. Kang, D. Shin, S. Bae, B. H. Hong, *Nanoscale* **2012**, *4*, 5527-5537.

[76] C. Cheng, S. Li, A. Thomas, N. A. Kotov, R. Haag, *Chem. Rev.*

2017, *117*, 1826-1914.

[77] L. Lin, B. Deng, J. Sun, H. Peng, Z. Liu, *Chem. Rev.* **2018**, *118*, 9281-9343.

[78] S. J. Park, O. S. Kwon, S. H. Lee, H. S. Song, T. H. Park, J. Jang, *Nano. Lett.* **2012**, *12*, 5082-5090.

[79] L. Wang, L. Wang, Y. Zhang, J. Pan, S. Li, X. Sun, B. Zhang, H. Peng, *Adv. Funct. Mater.* **2018**, *28*.

[80] S. Yang, F. Zhang, Q. Liang, Z. Wang, *Biosens. Bioelectron.* **2018**, *120*, 85-92.

[81] A. Canal-Martin, J. Sastre, M. J. Sanchez-Barrena, A. Canales, S. Baldominos, N. Pascual, L. Martinez-Gonzalez, D. Molero, M. E. Fernandez-Valle, E. Saez, P. Blanco-Gabella, E. Gomez-Rubio, S. Martin-Santamaria, A. Saiz, A. Mansilla, F. J. Canada, J. Jimenez-Barbero, A. Martinez, R. Perez-Fernandez, *Nat. Commun.* **2019**, *10*, 2798.

[82] L. Wang, W. A. Daoud, *Nano Energy* **2019**, *66*.

[83] S. Chen, Y. Song, D. Ding, Z. Ling, F. Xu, *Adv. Funct. Mater.* **2018**, *28*.

[84] Y. Zhao, Y. Yang, L. Cui, F. Zheng, Q. Song, *Biosens. Bioelectron.* **2018**, *117*, 53-59.

[85] Y. Jiang, N. Tang, C. Zhou, Z. Han, H. Qu, X. Duan, *Nanoscale* **2018**, *10*, 20578-20586.

[86] S. Chun, I. Y. Choi, W. Son, G. Y. Bae, E. J. Lee, H. Kwon, J.

Jung, H. S. Kim, J. K. Kim, W. Park, *Adv. Funct. Mater.* **2018**, *28*.

[87] B. Hatamluyi, F. Lorestani, Z. Es'haghi, *Biosens. Bioelectron.* **2018**, *120*, 22-29.

[88] H. Yoon, J. Jang, *Adv. Funct. Mater.* **2009**, *19*, 1567-1576.

[89] S. R. Ahn, J. H. An, H. S. Song, J. W. Park, S. H. Lee, J. H. Kim, J. Jang, T. H. Park, *ACS Nano* **2016**, *10*, 7287-7296.

[90] W. Fu, L. Feng, G. Panaitov, D. Kireev, D. Mayer, A. Offenhäusser, H.-J. Krause, *Sci. Adv.* **2017**, *3*, e1701247.

[91] O. S. Kwon, H. S. Song, S. J. Park, S. H. Lee, J. H. An, J. W. Park, H. Yang, H. Yoon, J. Bae, T. H. Park, J. Jang, *Nano. Lett.* **2015**, *15*, 6559-6567.

[92] S. G. Kim, J. S. Lee, J. Jun, D. H. Shin, J. Jang, *ACS Appl. Mater. Interfaces* **2016**, *8*, 6602-6610.

[93] T. T. K. Nguyen, T. N. Nguyen, G. Anquetin, S. Reisberg, V. Noel, G. Mattana, J. Touzeau, F. Barbault, M. C. Pham, B. Piro, *Biosens. Bioelectron.* **2018**, *113*, 32-38.

[94] X. Wang, G. Sun, P. Routh, D. H. Kim, W. Huang, P. Chen, *Chem. Soc. Rev.* **2014**, *43*, 7067-7098.

[95] J. S. Lee, S. G. Kim, J. Jun, D. H. Shin, J. Jang, *Adv. Funct. Mater.* **2014**, *24*, 6145-6153.

[96] J. Jun, J. S. Lee, D. H. Shin, J. Jang, *ACS Appl. Mater. Interfaces* **2014**, *6*, 13859-13865.

[97] S. J. Park, H. S. Song, O. S. Kwon, J. H. Chung, S. H. Lee, J. H.

An, S. R. Ahn, J. E. Lee, H. Yoon, T. H. Park, J. Jang, *Sci. Rep.* **2014**, *4*, 4342.

[98] N. Guajardo, C. Carlesi, Á. Aracena, *ChemCatChem* **2015**, *7*, 2451-2454.

[99] R. Zhang, S. He, C. Zhang, W. Chen, *J. Mater. Chem.B* **2015**, *3*, 4146-4154.

[100] J. P. Fruehauf, F. L. Meyskens, Jr., *Clin. Cancer Res.* **2007**, *13*, 789-794.

[101] M. Liu, Y.-X. Yu, W.-D. Zhang, *Electroanalysis* **2017**, *29*, 305-311.

[102] B. Halliwell, in *eLS*, **2015**, pp. 1-9.

[103] E. L. McAdam, T. J. Brodribb, S. A. McAdam, *Plant Cell Environ.* **2017**, *40*, 741-747.

[104] Y. F. Huan, Q. Fei, H. Y. Shan, B. J. Wang, H. Xu, G. D. Feng, *Analyst* **2015**, *140*, 1655-1661.

[105] X. Li, X. Du, *Sens. Actuators B-Chem.* **2017**, *239*, 536-543.

[106] E. Lindberg, N. Winssinger, *Chembiochem* **2016**, *17*, 1612-1615.

[107] M. Parrilla, R. Cánovas, F. J. Andrade, *Electroanalysis* **2017**, *29*, 223-230.

[108] R. J. Barst, *J. Clin. Invest.* **2005**, *115*, 2691-2694.

[109] M. Lassila, T. J. Allen, Z. Cao, V. Thallas, K. A. Jandeleit-Dahm, R. Candido, M. E. Cooper, *Arter. Thromb. Vasc. Biol.* **2004**, *24*, 935-942.

[110] K. Hosaka, Y. Yang, T. Seki, M. Nakamura, P. Andersson, P. Rouhi, X. Yang, L. Jensen, S. Lim, N. Feng, Y. Xue, X. Li, O. Larsson, T. Ohhashi, Y. Cao, *Nat. Commun.* **2013**, *4*, 2129.

[111] H. Qian, Y. Huang, X. Duan, X. Wei, Y. Fan, D. Gan, S. Yue, W. Cheng, T. Chen, *Biosens. Bioelectron.* **2019**, *140*, 111350.

[112] T. E. Lin, W. H. Chen, Y. C. Shiang, C. C. Huang, H. T. Chang, *Biosens. Bioelectron.* **2011**, *29*, 204-209.

[113] J. S. Lee, O. S. Kwon, D. H. Shin, J. Jang, *J. Mater. Chem. A* **2013**, *1*.

[114] R. Kim, J. S. Jang, D. H. Kim, J. Y. Kang, H. J. Cho, Y. J. Jeong, I. D. Kim, *Adv. Funct. Mater.* **2019**, *29*.

[115] A. Thiha, F. Ibrahim, S. Muniandy, I. J. Dinshaw, S. J. Teh, K. L. Thong, B. F. Leo, M. Madou, *Biosens. Bioelectron.* **2018**, *107*, 145-152.

[116] M. S. Yao, X. J. Lv, Z. H. Fu, W. H. Li, W. H. Deng, G. D. Wu, G. Xu, *Angew. Chem. Int. Ed.* **2017**, *56*, 16510-16514.

[117] O. S. Kwon, S. J. Park, H. Yoon, J. Jang, *Chem. Commun.* **2012**, *48*, 10526-10528.

[118] S. Holdren, R. Tsyshevsky, K. Fears, J. Owrutsky, T. Wu, X. Wang, B. W. Eichhorn, M. M. Kuklja, M. R. Zachariah, *ACS Catal.***2018**, *9*, 902-911.

[119] H. Yu, T. Szilvási, P. Rai, R. J. Twieg, M. Mavrikakis, N. L. Abbott, *Adv. Funct. Mater.* **2018**, *28*.

[120] V. Kumar, G. Raviraju, H. Rana, V. K. Rao, A. K. Gupta, *Chem. Commun.* **2017**, *53*, 12954-12957.

[121] Q. Han, L. Yang, Q. Liang, M. Ding, *Carbon* **2017**, *122*, 556-563.

[122] V. Rajendran, A. M. V. Mohan, M. Jayaraman, T. Nakagawa, *Nano Energy* **2019**, *65*.

[123] A. B. Patil, Y. Huang, L. Ma, R. Wu, Z. Meng, L. Kong, Y. Zhang, W. Zhang, Q. Liu, X. Y. Liu, *Biosens. Bioelectron.* **2019**, *142*, 111595.

[124] H. Yuan, T. Lei, Y. Qin, R. Yang, *Nano Energy* **2019**, *59*, 84-90.

[125] Y. Cheng, D. Wu, S. Hao, Y. Jie, X. Cao, N. Wang, Z. L. Wang, *Nano Energy* **2019**, *64*.

[126] K. K. Kim, I. Ha, P. Won, D. G. Seo, K. J. Cho, S. H. Ko, *Nat. Commun.* **2019**, *10*, 2582.

[127] J. S. Lee, J. Jun, S. Cho, W. Kim, J. Jang, *RSC Adv.* **2017**, *7*, 201-207.

[128] J. Cherusseri, K. K. Kar, *J. Mater. Chem. A* **2016**, *4*, 9910-9922.

[129] T.-L. Hsieh, H.-W. Chen, C.-W. Kung, C.-C. Wang, R. Vittal, K.-C. Ho, *J. Mater. Chem.* **2012**, *22*.

[130] Y. Lei, B. Liu, J. Lu, R. J. Lobo-Lapidus, T. Wu, H. Feng, X. Xia, A. U. Mane, J. A. Libera, J. P. Greeley, J. T. Miller, J. W. Elam, *Chem. Mater.* **2012**, *24*, 3525-3533.

[131] X. Qiu, H. Zhang, P. Wu, F. Zhang, S. Wei, D. Sun, L. Xu, Y. Tang, *Adv. Funct. Mater.* **2017**, *27*.

[132] G. H. Jeong, S. H. Kim, M. Kim, D. Choi, J. H. Lee, J. H. Kim, S. W. Kim, *Chem. Commun.* **2011**, *47*, 12236-12238.

[133] J.-G. Li, C.-Y. Tsai, S.-W. Kuo, *Polymers* **2014**, *6*, 1794-1809.

[134] J. M. Jeon, T. L. Kim, Y. S. Shim, Y. R. Choi, S. Choi, S. Lee, K. C. Kwon, S. H. Hong, Y. W. Kim, S. Y. Kim, M. Kim, H. W. Jang, *Adv. Mater.* **2017**, *29*.

[135] H. Yoon, J. H. Kim, N. Lee, B. G. Kim, J. Jang, *Chembiochem* **2008**, *9*, 634-641.

[136] H. Yoon, S. Ko, J. Jang, *J. Phys. Chem. B***2008**, *112*, 9992-9997.

[137] J. Yang, X. Qian, H. Li, H. Wang, X. Xue, L. Cai, P. Hu, G. Yu, *Adv. Mater. Interfaces* **2018**, *5*.

[138] H. Wang, E. Gao, P. Liu, D. Zhou, D. Geng, X. Xue, L. Wang, K. Jiang, Z. Xu, G. Yu, *Carbon* **2017**, *121*, 1-9.

[139] D. Mardiansyah, T. Badloe, K. Triyana, M. Q. Mehmood, N. Raeis-Hosseini, Y. Lee, H. Sabarman, K. Kim, J. Rho, *Sci. Rep.* **2018**, *8*, 10639.

[140] S. Elzey, J. Baltrusaitis, S. Bian, V. H. Grassian, *J. Mater. Chem.***2011**, *21*.

[141] R. Betancourt-Galindo, P. Y. Reyes-Rodriguez, B. A. Puente-Urbina, C. A. Avila-Orta, O. S. Rodríguez-Fernández, G. Cadenas-Pliego, R. H. Lira-Saldivar, L. A. García-Cerda, *J. Nanomater.* **2014**, *2014*, 1-5.

[142] Y. Lin, K. A. Watson, M. J. Fallbach, S. Ghose, J. Joseph G.

Smith, D. M. Delozier, W. Cao, R. E. Crooks, J. W. Connell, *ACs Nano* **2009**, *3*, 871-884.

[143] Y. Cao, H. Lu, Q. Hong, B. Xu, J. Wang, Y. Deng, W. Yang, W. Cai, *Carbon* **2019**, *144*, 280-288.

[144] K. D. Park, M. B. Raschke, J. M. Atkin, Y. H. Lee, M. S. Jeong, *Adv. Mater.* **2017**, *29*.

[145] X. Chen, R. Xiang, P. Zhao, H. An, T. Inoue, S. Chiashi, S. Maruyama, *Carbon* **2016**, *107*, 852-856.

[146] R. Wang, D. Lu, H. Bai, C. Jin, G. Yan, M. Ye, L. Qiu, R. Chang, C. Cui, H. Liang, W. Tan, *Chem. Sci.* **2016**, *7*, 2157-2161.

[147] H. H. Lee, P. A. Lim, H. Vu, S.-A. Poulsen, L. R. Gahan, *Polyhedron* **2015**, *85*, 627-634.

[148] Y. Xiong, Y. Chen, L. Ding, X. Liu, H. Ju, *Analyst* **2019**, *144*, 4545-4551.

[149] C. Przybylski, V. Bonnet, R. R. Vives, *Chem. Commun.***2019**, *55*, 4182-4185.

[150] J. S. Lee, W. Kim, S. Cho, J. Jun, K. H. Cho, J. Jang, *J. Mater. Chem. B* **2016**, *4*, 4447-4454.

[151] Z. Yang, J. Lv, H. Pang, W. Yan, K. Qian, T. Guo, Z. Guo, *Sci. Rep.* **2015**, *5*, 17473.

[152] X. Wang, B. D. Myers, J. Yan, G. Shekhawat, V. Dravid, P. S. Lee, *Nanoscale* **2013**, *5*, 4119-4122.

[153] X. Zhao, Y. Hou, Y. Wang, L. Yang, L. Zhu, R. Cao, Z. Sha, *RSC*

Adv. **2017**, *7*, 40286-40294.

[154] J. Zhang, Y. Li, L. Wang, C. Zhang, H. He, *Catal. Sci. Technol.* **2015**, *5*, 2305-2313.

[155] S. Liang, F. Teng, G. Bulgan, R. Zong, Y. Zhu, *J. Phys. Chem. B* **2008**, *112*, 5307-5315.

[156] S. Ozcan, A. Guler, T. Cetinkaya, M. O. Guler, H. Akbulut, *Beilstein J. Nanotechnol.***2017**, *8*, 1932-1938.

[157] J. Wu, Z. Wu, S. Han, B. R. Yang, X. Gui, K. Tao, C. Liu, J. Miao, L. K. Norford, *ACS Appl. Mater. Interfaces* **2019**, *11*, 2364-2373.

국문초록

최근, 높은 종횡비 및 비표면적과 같은 구조적 특성으로 인해 센서 트랜스듀서 물질로 1차원 나노물질을 이용하는 연구가 활발하게 진행되고 있다. 1D 나노 물질을 제조하는 다양한 방법 중, 전기 방사는 간단한 사용법과 낮은 작동 온도 때문에 널리 사용되어왔다. 또한, 제조 된 섬유는 매트 형태로되어 있기 때문에, 그 자체적으로 다양한 응용에 적용이 가능하다는 장점을 지닌다. 전기 방사를 통해 1D 나노 물질을 제조하기위한 다양한 합성 방법이 연구되어 왔지만, 나노 섬유에 금속 또는 금속 산화물의 도입해 복합나노재료를 만들거나 나노섬유를 탄화 후 유연하게 유지하는 방법에 대한 연구는 미진하다.

이 논문은 금속, 금속산화물 또는 탄소 소재를 전기방사 폴리아크릴로니트릴 나노섬유에 도입해 복합재료를 제조하는 방법에 대한 연구를 기술하였다. 우선, 폴리아크릴로니트릴 용액을 전기 방사해 제조한 나노섬유에 기상 증착 중합으로 폴리피롤을 코팅하였고, 이를 작동전극으로 하여 형상을 제어한 팔라듐 나노 플라워를 전기도금 방법을 이용해 도입하였다. 팔라듐의 형상은 전기도금 시 사용하는

전해질에서 황산 농도를 조절함으로써 결정되었다. 이렇게 제조한 물질은 과산화수소 센서 전극 재료로서 적용되었다.

두번째로, 화학 기상 증착 및 금속 식각 방법은 탄소 나노 섬유 상에 구리를 이용해 제조한 탄소를 도입하기 위해 사용하였다. 구리를 이용해 제조한 탄소의 구조는 사용한 구리 형상 종류에 의해 결정되었다. 그중 구 형상 구리를 사용했을 때 탄소나노 섬유 상에 돌기 형태의 탄소를 도입 할 수 있었다. 제조한 물질에 혈소판 유래 성장 인자 (PDGF) 결합 압타머를 고정시켜, 높은 감도 및 선택성을 갖는 바이오 센서로서 적용 하였다.

마지막으로, 이산화망간을 도입한 탄소나노섬유를 제조하기 위해, 과망간산 칼륨을 전구체로 사용하고 열처리 및 교반을 이용해 화학적으로 환원시켰다. 제조한 물질은, 신경 유도체인 디메틸 메틸포스포네이트 분자 검출용 화학센서의 트랜스듀서 물질로 적용하였다.

또한 이 논문에서 제조한 물질이 굽힘에도 불구하고 저하되지 않는 전기 저항 및 타겟 분석물질 감지 성능을 나타낸다는 사실을 통해 유연하고 독립된 기판 센서 물질로 활용 할 가능성을 제공하였다.

주요어: 폴리아크릴로니트릴; 전기방사; 1차원 나노물질; 탄소나노섬유; 폴리피롤; 센서

학 번: 2015-21014

감사의글

이 공학박사 학위논문이 완성되기까지 지난 5년간 많은 분들께서 도와주시고 신경 써 주셨습니다. 그 고마운 분들께 짧은 글로나마 감사의 인사를 드리며 논문을 마무리 하고자 합니다.

먼저 5년간 부족한 저를 지도해주신 장정심교수님께 감사의 말씀 드리고 싶습니다. 교수님 보시기에 부족한 점이 많았던 제자였음에도 불구하고 너그러운 마음으로 기다리며 지도해 주신 덕분에 박사학위를 받을 수 있지 않았나 싶습니다. 연구 지도뿐만 아니라 인생에서 살면서 갖추어야 할 부분들을 행동으로 보여주신 교수님의 가르침을 잊지 않고, 사회에 공헌하는 사람이 되도록 하겠습니다. 또한 바쁘신 와중에도 부족한 제 학위 심사를 맡아주신 조재영교수님, 이종찬 교수님, 오준학교수님 그리고 임순호 박사님께 이 글을 빌어 감사의 말씀을 전합니다.

다음으로 학위기간동안 실험실에서 함께 생활했던 많은 선/후배 분들께 감사드립니다. 우선 졸업 전, 후에도 많은 도움을 준 준섭이형, 사수는 아니지만 많은 것을 알려준 동훈이형과 재문이형, 같은 팀으로 함께했던 지현이형, 진욱이형, 정균이

형, 경희누나, 고은누나에게도 고맙다고 전하고 싶습니다. 졸업을 같이 준비한 원래 선배, 졸업 동기 윤기형과 동기인 원주형 덕분에 디펜스 준비 과정이 즐거웠던 것 같아 감사의 인사를 전합니다. 각자 졸업 후 진로가 다르지만 원하는 앞날을 이룰 수 있기를 바라겠습니다. 또한 연구실 마지막쯤을 같이 하며 고생한 성근이형, 해준이형, 경섭이형, 중원이형, 예리에게도 감사의 말씀을 전합니다. 그 외에 연구실 생활을 연구적, 생활적으로 도와주셨던 재훈이형, 정섭이형, 주영이형에게 고맙습니다. 마지막으로 석사 졸업을 해서 2년간만 같이 했지만 동기였던 노정철, 양희경에게도 감사의 말씀을 전합니다.

마지막으로 지금까지 키워주시고 보살펴주신 부모님과, 동생에게 깊은 감사의 말씀을 드리고 싶습니다. 어렸을 때부터 항상 기도해주신 덕분에 본 학위를 잘 마무리 할 수 있었던 것 같습니다. 마찬가지로 항상 저를 위해 기도해주시는 두분 할머니들이 계셔서 9년이라는 긴 대학교 생활을 잘 마무리 할 수 있었던 것 같아 깊이 감사드립니다.

감사의 글을 작성하며 지난 5년간 많은 분들과 새로운 인연을 맺으며 도움을 받았다는 사실에 행복한 대학원 생활을 했다는 생각이 듭니다. 연구실에서 얻은 경험을 큰 밑거름으로 삼아 학위를 주신 교수님 명성에 누가되지 않게, 스스로에게

부끄럽지 않은 박사가 되도록 노력하겠습니다.

그동안 감사했습니다.

2020년 2월

관악을 내려가며

김우영 올림